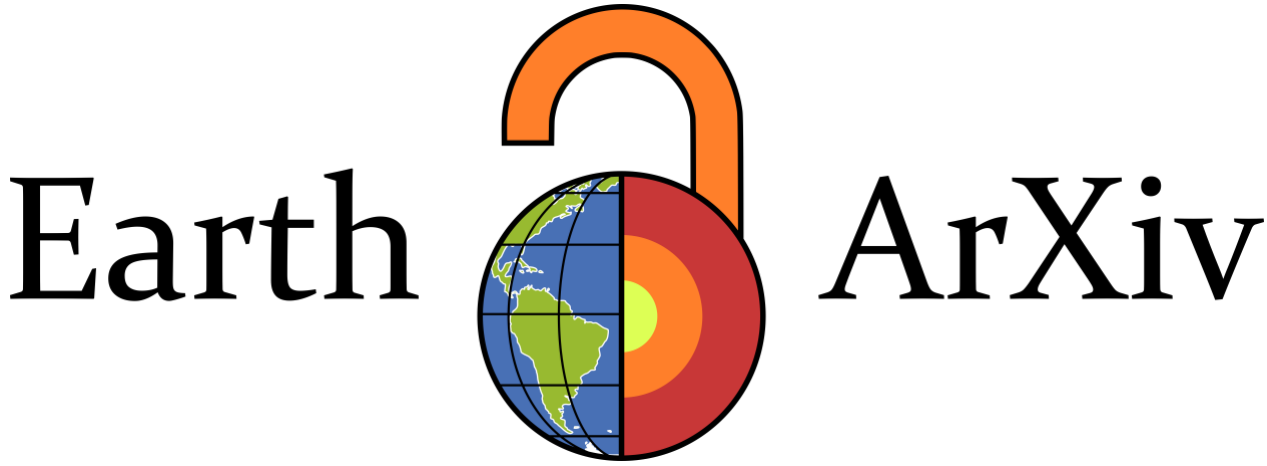


This is a non-peer-reviewed preprint submitted to EarthArXiv.

This manuscript has been submitted for publication in *Journal of Glaciology*. Please note the manuscript has yet to be formally accepted for publication. Subsequent versions of this manuscript may have slightly different content. If accepted, the final version of this manuscript will be available via the 'Peer-reviewed Publication DOI' link on the right-hand side of this webpage. Please feel free to contact any of the authors; we welcome feedback.

Surface signatures of surge dynamics over six decades at Tweedsmuir Glacier, Saint Elias Mountains, Canada

Meghan A. SHARP,[1,2] Dan H. SHUGAR,[1], Gwenn E. FLOWERS,[3] Aram FATHIAN,[1] Friedrich KNUTH[4,5]

[1] *Water, Sediment, Hazards and Earth-surface Dynamics (WaterSHED) Laboratory, Department of Earth, Energy, and Environment, University of Calgary, Calgary, Alberta, Canada;* [2] *Present address: College of Earth, Ocean, and Atmospheric Science, Oregon State University, Corvallis, OR, USA;* [3] *Department of Earth Sciences, Simon Fraser University, Burnaby, British Columbia, Canada;* [4] *Laboratory of Hydraulics, Hydrology and Glaciology (VAW), ETH Zurich, Zurich, Switzerland;* [5] *Swiss Federal Institute for Forest, Snow and Landscape Research (WSL), bâtiment ALPOLE, Sion, Switzerland;*
Correspondence: Meghan A. Sharp <sharpmeg@oregonstate.edu>

ABSTRACT.
The dynamically driven advance and retreat of surge-type glaciers shapes surrounding ecosystems and landscapes differently from non-surging glaciers; however, the diversity in surge behaviour, even among neighbouring glaciers, makes them challenging to predict. Here, we reconstruct the six-decade surge history of Tweedsmuir Glacier in the Saint Elias Mountains, capturing two surge cycles. We use historical and satellite images to document rates of ice-thickness change, surface slope, cycle length, dynamic balance line position, and terminus advance and retreat between 1950 and 2010. Additionally, spectral analysis of the reconstructed glacier surfaces confirms that surface topography is amplified during and immediately following surges. Collectively, these proxies indicate that either the surge cycle lengthened over the study period, or the most recent surge (2007–2009) initiated with a lower driving stress than the preceding one (1973). While the glacier historically contacted the river during surges, terminus retreat has likely reduced the hazard of ice-damming. This study extends the known surge record of Tweedsmuir Glacier by two-and-a-half decades and provides a new proxy for distinguishing surge and quiescent phases from historical DEMs, multidecadal validation data to test theories of glacier surging, and a potential test site for improved bed-topography inversions that leverage high-slip regimes.

INTRODUCTION

Mountain glaciers are actively reshaping landscapes, habitats, and water resources across the planet due to sustained periods of negative net mass balance driven by climate warming. However, some glaciers undergo dynamically-driven cycles of advance and retreat that are decoupled from climate forcing. Glacier surges are short episodes of fast flow on timescales of years to decades (the active surge phase) triggered by changes in the subglacial thermal and/or hydrological state, and followed by longer periods of slow flow (the quiescent phase) (e.g. Meier and Post, 1969; Clarke and others, 1984; Kamb and others, 1985; Raymond, 1987; Dowdeswell and others, 1991; Björnsson, 1998). This rapid transport of mass from a reservoir that accumulates over years–centuries to a lower-lying receiving zone often results in a terminus advance and poses unique hazards to human activity and ecosystems, such as ice dams and their associated glacial lake outburst floods (e.g. Post and Mayo, 1971; Hewitt and Liu, 2010; Clague and Rampton, 2011; Bhambri and others, 2019; Kochtitzky and others, 2020). Additionally, the high-slip regime of surges has been used as an analog for understanding fast flow at outlet glaciers on the polar ice sheets (e.g. Doyle and others, 2018; Young and others, 2019), and been proposed as a natural laboratory to improve inversions of bed topography (Morin and others, 2023).

Many surge-type glaciers exist in an optimal climatic envelope between "cold and dry" and "warm and temperate" end members (Sevestre and Benn, 2015; Benn and others, 2019), suggesting that climate exerts a first-order control on the global distribution of surge clusters and an indirect control on surge dynamics. Several studies corroborate a relationship between mass balance and surge behaviour (Lovell and others, 2026), whereby diminishing accumulation in the reservoir zone leads to a decrease in the maximum terminus extent (Eisen and others, 2005; Bevington and Copland, 2014;

Kochtitzky and others, 2019, 2020) and flow velocity (Frappé and Clarke, 2007; De Paoli and Flowers, 2009) attained during surges, and in the most extreme case, the cessation of surges altogether (e.g. Dowdeswell and others, 1995). The length of a surge cycle may also adjust to the accumulation rate preceding the surge, and is generally thought to lengthen with decreasing net balance (Eisen and others, 2001), although some glaciers exhibit relatively consistent (Kochtitzky and others, 2020) or even shortened intervals under decreasing negative mass balance (Bevington and Copland, 2014). However, the ability of a glacier to accumulate a sufficient reservoir can also be modulated dynamically by spatial variations in bed topography and composition (Fowler and others, 2001; Flowers and others, 2011; Crompton and others, 2018; Lovell and others, 2018; Nolan and others, 2021; Liu and others, 2024). This variable interplay between climate and glacier dynamics contributes to the diversity of surge behaviour and makes it challenging to understand how surge-type glaciers will respond to climate change (Lovell and others, 2026), motivating the need for multidecadal observations at the scale of individual glaciers.

Furthermore, surge-type glaciers interact with surrounding ecosystems in ways that differ from non-surging glaciers. Notably, terminus advances during surges of Nàłùdäy (Lowell Glacier) in southwestern Yukon in have created an ice dam across the Alsek River several times in the past 1000 years, leading to catastrophic flooding upstream and blocking ecologically and culturally important sockeye salmon migrations (Lindsey, 1975; Holdsworth and others, 2002; Clague and Rampton, 2011). However, geomorphic evidence suggests that since the late 1800s, none of the glaciers in the Alsek watershed (including Nàłùdäy) have blocked the river (Clague and Rampton, 2011). Despite the absence of an ice-dam, sockeye salmon have not returned to the upper watershed.

It has been postulated that the neighbouring Tweedsmuir Glacier, located down-river from Nàłùdäy, may be an important control on the present-day configuration of the Alsek River (Champagne & Ashihik First Nations, 2006; Shugar and others, 2024). The terminus of Tweedsmuir Glacier abuts a ridge, forcing the Alsek River through a narrow bedrock canyon—a notorious section of rapids known as "Turnback Canyon" (Figure 1) that may be a remaining barrier to migrating fish. Thus, an advance or retreat of Tweedsmuir Glacier could alter the course of the Alsek River and directly impact anadromous fish in the Alsek watershed. Yet, little is known about the dynamics and surge history of Tweedsmuir Glacier, let alone its future.

This study has two complimentary motivations: advancing our understanding of the interplay between climate and surge dynamics from remotely-sensed observations of the glacier surface, and characterizing the evolution of the culturally- and ecologically-significant Tweeedsmuir Glacier. We begin by documenting key characteristics of surges of Tweedsmuir Glacier between 1950 and 2010—the rate of change of ice thickness, surface slope, cycle length, and terminus advance/ retreat. We then use spectral analysis to quantify the amplification of glacier surface topography during surges relative to quiescent phases, corroborating prior theory (Gudmundsson, 2003). We focus our discussion on how surge behaviour has changed across cycles, and show that several proxies (e.g. changes in surface slope, ice thickness, terminus position, and the amplitude of surface topography) indicate either a lengthening of the surge cycle, or a decrease in the critical driving stress at which surges initiate.

STUDY SITE AND SURGE HISTORY OF TWEEDSMUIR GLACIER

Tweedsmuir Glacier is a surge-type valley glacier in the Saint Elias Mountains (Figure 1), a high coastal mountain range between southwestern Yukon, northwestern British Columbia, and Southeast Alaska, with a high density of surge-type glaciers. Of the 204 surge-type glaciers identified in western North America by Post (1969), 136 of them are found here. On the traditional territories of the Champagne and Aishihik First Nations, Tweedsmuir Glacier is one of the largest glaciers in the Canadian portion of the Saint Elias Mountains. It spans elevations between approximately 200 and 2800 m a.s.l. (RGI 7.0 Consortium, 2023). Covering a total area of 592 km^2 (RGI 7.0 Consortium, 2023), the glacier is $\sim$80 km long, $\sim$3.5 km wide along the main trunk, and spreads into an 8.5 km-wide piedmont lobe at its terminus. Based on airborne ice-penetrating radar observations from NASA'S Operation IceBridge (MacGregor and others, 2021) and unpublished ground and helicopter-based ice-penetrating radar data collected in July 2022, there is a 10 km-long overdeepening beneath the piedmont lobe (Tober and others, 2026), which reaches a maximum ice thickness of 500 m (Figure 3 a,b). The upstream end of the lobe is bordered by a $\sim$ 100 m-tall basal ridge (grey arrows in Figure 3 a,b), beyond which the basal topography is unknown.

Two surges of Tweedsmuir Glacier have previously been observed. The first initiated in early 1973 ("Surge 1"), reaching peak activity in June–July and terminated by the end of the year or in early 1974 (Holdsworth and others, 2002; Krimmel and Meier, 1975). Surface velocities during this time were estimated by measuring the displacement of medial moraines in the terminal piedmont lobe. Based on these

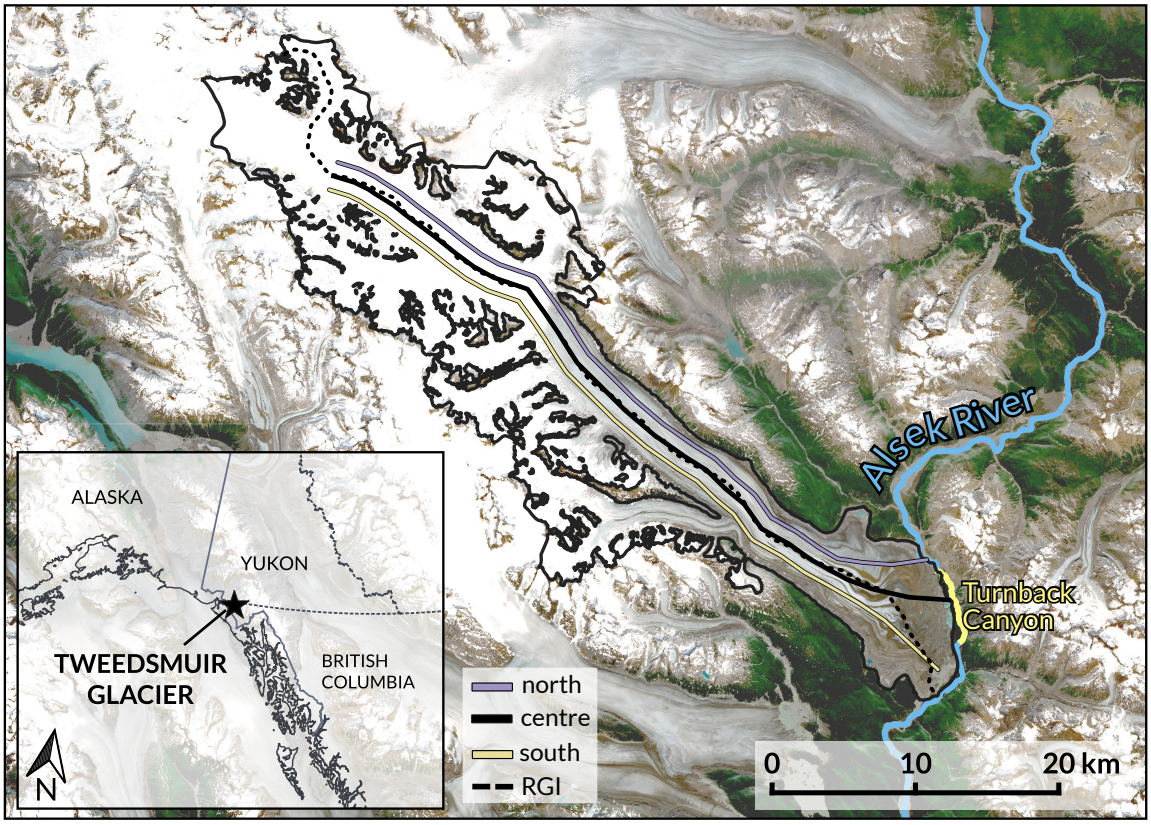


Fig. 1. Map of Tweedsmuir Glacier, Alsek River, Turnback Canyon, and elevation profiles used in this study. The GLIMS glacier polygon (Raup and others, 2007) is outlined in black and the RGI (RGI 7.0 Consortium, 2023) centreline is shown in a dashed black line. Inset: Location of Tweedsmuir Glacier (orange star) in British Columbia, Canada. Background: Copernicus Sentinel-2 image acquired on 14 August 2026.

estimates, surface speeds during the active surge phase exceeded 10 m day^{-1} between late July and mid September, 1973 (Krimmel and Meier, 1975), and decreased by an order of magnitude to 1 m day^{-1} in late August, 1978 (Holdsworth and others, 2002), at the beginning of the quiescent phase. During the winter of 1973–74, Tweedsmuir Glacier temporarily dammed the Alsek River (Holdsworth and others, 2002).

The second observed surge of Tweedsmuir Glacier began sometime before October, 2007 and was completed by June, 2009 ("Surge 2") (National Park Service, 2015). Based on ITS_LIVE velocity measurements (Supplementary Figure S1; Gardner and others, 2024), the terminal lobe of the glacier reached a peak velocity of 11 m day^{-1} in April, 2008. This surge is not as well studied, scientifically, as the first, but was monitored by the U.S. National Park Service (National Park Service, 2015) due to the risk of an ice dam across the Alsek River. Observations suggest that the glacier contacted the Alsek River again in August of 2008, but did not create an ice dam.

DATA AND METHODS

We produced and compiled a six-decade record of Digital Elevation Models (DEMs) of Tweedsmuir Glacier derived from historical and satellite imagery. We subtracted the DEMs to quantify elevation changes over the two observed surge cycles, tracked terminus advance and retreat with the orthomosaics, and applied techniques from spectral analysis to compare the glacier-surface topography between surge and quiescent phases.

The surface elevations of Tweedsmuir Glacier were reconstructed for 1950, 1969, 1974, 1979, and 1987 from scanned historical air photographs (Supplementary Figure S2), and 2007, 2009, and 2010 from SPOT-5 satellite stereopairs. We acquired an additional publicly-available Shuttle Radar Topography Mission (SRTM) satellite DEM from 2000. Although these timestamps were dictated by data availabil-

Table 1. Timeline of historical and satellite DEMs. Shaded rows denote active surge phases.

Date	Surge [a] Phase	DEM [b] Source	Pixel Size (m)	Vertical [c] Accuracy (m)
1950	?	HSfM	2	13.0
1969	Q	HSfM	2	3.2
1974	**S1**	**HSfM**	**2**	**5.7**
1979	Q	HSfM	2	4.8
1987	Q	HSfM	2	3.6
2000	Q	SRTM	30	5.7
2007	**S2**	**SPOT-5**	**12**	**10.2**
2009	**S2**	**SPOT-5**	**12**	**11.6**
2010	Q	SPOT-5	12	13.1
2009–2021	*Reference*	*ArcticDEM v4.1*	*2*	*2–12*

[a]Quiescent and active surge phases are denoted by "Q" and "S", respectively.

[b]DEM sources marked as "HSfM" are produced from historical images and "SPOT-5" are produced from stereo-pairs in this study. Shuttle Radar Topography Mission (SRTM) is a publicly available DEM product.

[c]Vertical accuracy is the normalized Median Absolute Deviation (nMAD) relative to the reference DEM (see text for details).

ity, they are well distributed throughout different phases of the surge cycle (Table 1). The earliest snapshots, 1950 and 1969, provide insight prior to previously-documented observations (Figure 2). The first observed surge in 1973 (Holdsworth and others, 2002) is bracketed by the 1969 and 1974 DEMs. The next three timestamps, 1979, 1987 and 2000, cover the subsequent quiescent period. The 2007, 2009, and 2010 snapshots bracket the second observed surge (2007–2009) (National Park Service, 2015) and mark the end of a complete surge cycle.

Historical DEM generation

Historical images and initial camera metadata

Historical images were acquired by the Royal Canadian Air Force and Austin Post/ US Geological Survey, and obtained from three collections: the Canadian National Air Photo Library (1950: 85 images, 1979: 29 images), the North American Glacier Aerial Photography (NAGAP) Archive (1974: 16 images, Nolan and others, 2017), additional NAGAP images scanned by the University of Alaska Fairbanks for this study (1969: 16 images), and the province of British Columbia's GeoBC image library (1987: 22 images). Initial horizontal camera positions were manually estimated by locating the centre of each image in the ESRI World Imagery global basemap using QGIS v3.34.15 (Dawson and others, 2025). Vertical positions were estimated assuming a flight altitude of 1000 m above the National Elevation Dataset (United States Geological Survey, 2019) with camera orientations pitch, roll, and yaw set to 0° (nadir, heading north), as per the workflow described in Knuth and others (2023). Metadata for each image set, including the camera type, focal lengths, scanning resolutions, and distance between fiducial markers are summarized in Supplementary Table S1.

Image pre-processing

Historical images were pre-processed using the Historical Image Pre-Processing (HIPP) library (Knuth and others, 2021) to standardize the images and improve the camera model optimization during subsequent photogrammetric reconstruction. All images were enhanced with a contrast-limited adaptive histogram equalization and cropped around the principal point to remove the photo frame. When possible, we used fiducial markers to apply an affine transformation and remove distortion that can arise from film storage, handling, or scanning. Example raw images and fiducial markers are shown in Supplementary Figure S2, and camera metadata and fiducial marker distances are provided in Supplementary Table S1.

The 1950 image set was pre-processed with an affine transformation to match mean fiducial marker positions, following the workflow described by Knuth and others (2023), as no calibration reports were available. Fiducial markers were manually detected in each image using Agisoft Metashape v2.0.3—hereafter, "Metashape"—(Agisoft Metashape, 2023) and the average position of each marker was used to define the affine transformation with HIPP.

Like most images in the NAGAP archive, the 1969 and 1974 image sets do not have visible fiducial markers and lack calibration reports. Instead, notch patterns on the photo frame were used as "pseudofiducial markers" to estimate principal points. No affine transformation was applied when using pseudofiducial markers (Knuth and others, 2023).

The 1979 and 1987 image sets were pre-processed in HIPP using an affine transformation obtained from measured fiducial marker positions and their calibrated dimensions. Fiducial markers were automatically detected in Metashape and manually refined where necessary. For the 1979 imagery, calibrated fiducial positions were extracted from the corresponding camera calibration report. As no calibration report was available for the 1987 imagery, we instead used nominal fiducial coordinates compiled by McNabb (2025), derived from a collection of calibration reports for the same camera model (Wild RC8).

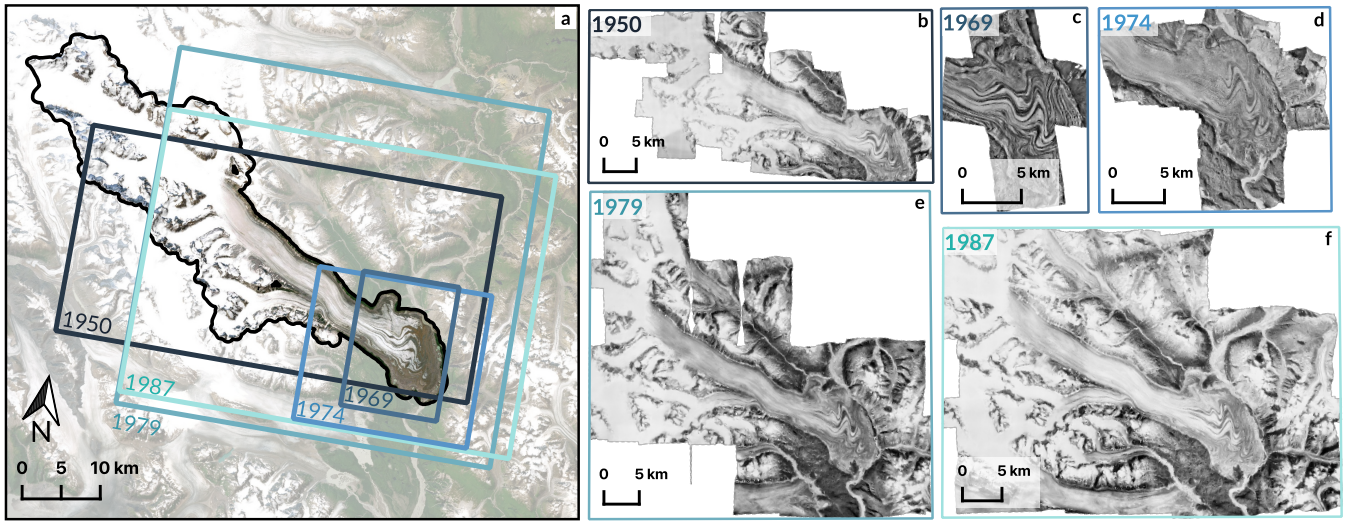


Fig. 2. Footprint of historical DEMs and orthomosaics produced in this study. Tweedsmuir Glacier is outlined in black by the GLIMS outline (Raup and others, 2007) with a 500 m buffer.

Four-dimensional Structure from Motion photogrammetry (4D SfM)

Structure from Motion (SfM) is a photogrammetric technique that builds three-dimensional point clouds from overlapping two-dimensional images. With the images standardized, we performed a two-step multi-temporal bundle adjustment using Historical Structure from Motion (HSfM)—a python-based automated pipeline for SfM photogrammetric reconstruction and DEM co-registration (Knuth and others, 2023). The HSfM workflow does not require the manual placement of ground control points to georeference the resulting point clouds and instead uses the estimated initial camera positions.

First, a joint bundle adjustment was performed, where all available images across all image sets (i.e. all acquisition dates) were processed together to optimize the camera models and produce a composite DEM. The composite DEM was then co-registered using HSfM's multi-stage co-registration procedure (Knuth and others, 2023), which applies a three-step Iterative Closest Point (ICP) alignment routine followed by the Nuth and Kääb (2011) DEM co-registration method for sub-pixel refinement. The resulting combined transform is then applied back to the bundle adjusted cameras to correct their absolute position and orientation. Next, the optimized camera models were used for photogrammetric reconstruction using each individual image set belonging to a single acquisition date. The intrinsic parameters from the multi-temporal optimization were held fixed during these bundle adjustment runs. Instead of employing the multi-stage HSfM co-registration procedure again for the single-date DEMs, we achieved better results with the Least Z Difference method (Rosenholm and Torlegård, 1988), which performs both a three-dimensional translation and rotation. We implemented the Least Z Difference co-registration with the Python library xDEM v0.2.0—hereafter, "xDEM"—(xDEM contributors, 2026). The co-registration process is described in detail below.

The final single-date DEMs were posted as 2 m resolution, which is greater than the ground sample distance computed for each bundle-adjusted image set and equal to the resolution of the reference DEM (ArcticDEM). Small data gaps in the DEMs were filled using the GDAL FillNodata algorithm (implemented via rasterio in Python), which interpolates missing pixels by inverse distance weighting of valid pixels found in a four-direction search, with a maximum search distance of 50 pixels (100 m). Using the initial camera-position estimates and the multi-temporal SfM approach described above, we produced DEMs with error estimates on the order of $\sim$ 10 m after final co-registration (Table 1, Supplementary Figure S3).

Satellite DEM generation

In addition to historical DEMs, we generated three DEMs of Tweedsmuir Glacier from stereoscopic images acquired by the High Resolution Stereoscopic (HRS) instrument onboard the SPOT-5 satellite. SPOT-5 HRS captures forward (HRS1) and backward (HRS2) viewing geometries in a single orbital pass (e.g. Toutin and others, 2011; Korona and others, 2009).

We processed three stereo pairs acquired between September 2007 and September 2010 (Table 1), covering a footprint of approximately 11 000 km^2. The DEMs were created using the NASA Ames Stereo Pipeline (Beyer and others, 2018; Shean and others, 2016), with a processing workflow consisting of: relative orientation, map projection, dense stereo matching, triangulation, and DEM rasterization.

First, we performed a relative bundle adjustment on the forward and backward images of each stereo pair to evaluate their internal geometric consistency (Beyer et al., 2018). Rational polynomial coefficient (RPC) camera models were subsequently generated from the SPOT-5 metadata and appended to the corresponding metadata files. To minimize disparity search ranges and reduce the impact of severe topographic distortions during the matching phase, we map-projected the forward and backward images onto the Copernicus GLO-30 reference surface using the RPC camera model (Beyer and others, 2018; Shean and others, 2016).

Dense stereo matching was performed on the map-projected pairs using a hybrid Semiglobal Matching (SGM)/More Global Matching (MGM) mode in which SGM is used at preceding resolution levels and MGM at the final resolution level (Hirschmuller, 2008; Facciolo and others, 2015; Beyer and others, 2018). Disparities were further refined using an affine-adaptive window correlation technique (Stein and others, 2006; Beyer and others, 2018). The refined disparities were triangulated to generate point clouds, which were subsequently rasterized into DEMs using ASP's *point2dem* utility (Beyer and others, 2018; Shean and others, 2016), producing final surface models with a grid spacing of approximately 12 m.

DEM co-registration

All DEMs were co-registered to ArcticDEM v4.1 (Porter and others, 2023), a 2 m-resolution mosaic DEM from strips collected between 2009 and 2021, using the Least Z Difference algorithm (Rosenholm and Torlegård, 1988) in xDEM. The horizontal and vertical accuracy of ArcticDEM is approximately 4 m (Polar Geospatial Center, 2026).

To exclude unstable terrain, i.e. terrain that undergoes changes on the timescale of the study period, we apply a stable-ground mask that only includes pixels classified as grassland and bare/ sparse vegetation in the ESA WorldCover v200 (Zanaga and others, 2022) global land cover map. We mask out all glaciers using the Global Land Ice Measurements from Space (GLIMS) glacier outlines (Raup and others, 2007) and apply a 100 m buffer to the outline of Tweedsmuir Glacier. Additionally, slopes greater than 45° are excluded from the reference DEM for co-registration (e.g. Nuth and Kääb, 2011; Knuth and others, 2023).

In order to remove systematic broad-scale errors in the 1979 and 1987 DEMs, which appear as "doming" effects in the residuals, we apply xDEM's deramping correction with a second-order polynomial to these two DEMs after co-registration. We report the vertical accuracy of the DEMs in Table 1 as the normalized Median Absolute Deviation (nMAD) of the residuals between the DEM and the reference ArcticDEM over stable terrain:

$$\mathrm{NMAD} = 1.4826\,\mathrm{median}(|\mathrm{dz_i} - \mathrm{m_{dz}}|)\,, \tag{1}$$

where $\mathrm{dz_i}$ are the individual errors, and $\mathrm{m_{dz}}$ is the median of the errors (Höhle and Höhle, 2009). Thus, the NMAD is an estimate of the standard deviation that is resilient to outliers and a robust measure of DEM accuracy (Höhle and Höhle, 2009). The histograms of residuals before and after co-registration are provided in Supplementary Figure S3.

Ice thickness change and surface slope

Driving stress exerts a key control on both the initiation and termination of surges (e.g. Clarke and others, 1984; Eisen and others, 2001; Liu and others, 2024; Terleth and others, 2024). Assuming longitudinal stress gradients are small (i.e. Shallow Ice Approximation), the glacier driving stress is

$$\tau_\mathrm{d} = \rho_\mathrm{i} \mathrm{g} \mathrm{H} \sin(\alpha)\,, \tag{2}$$

where ρ_i is the density of ice, g is gravitational acceleration, H is the ice thickness, and α is the glacier-surface slope (e.g. Cuffey and Paterson, 2010).

During quiescence, mass accumulates in the reservoir zone, thickening and steepening the glacier surface until the driving stress approaches a critical value and a surge begins (Clarke and others, 1984; Eisen and others, 2001; Liu and others, 2024). The surge then transfers mass from the reservoir to the receiving zone, thinning and flattening the reservoir and lowering its driving stress. Together with the evacuation of stored basal water, the reduction in driving stress eventually terminates the surge (Clarke and others, 1984; Terleth and others, 2024). While we do not have absolute ice thickness measurements to calculate the driving stress directly, we gain insight into changes in driving stress throughout the surge cycle by tracking changes in H and α.

The glacier-surface slope is tracked throughout the study period along a centerline. We extracted elevation profiles from each DEM, sampled every 30 m, and calculated the slope of the best-fitting first-order polynomial using a least-squares linear regression. We exclude the lower 3 km from the linear regression due to undulating topography in the terminal lobe (Figure 3 a,b). The centerline profile follows the Randolph Glacier Inventory (RGI) geometrical centerline

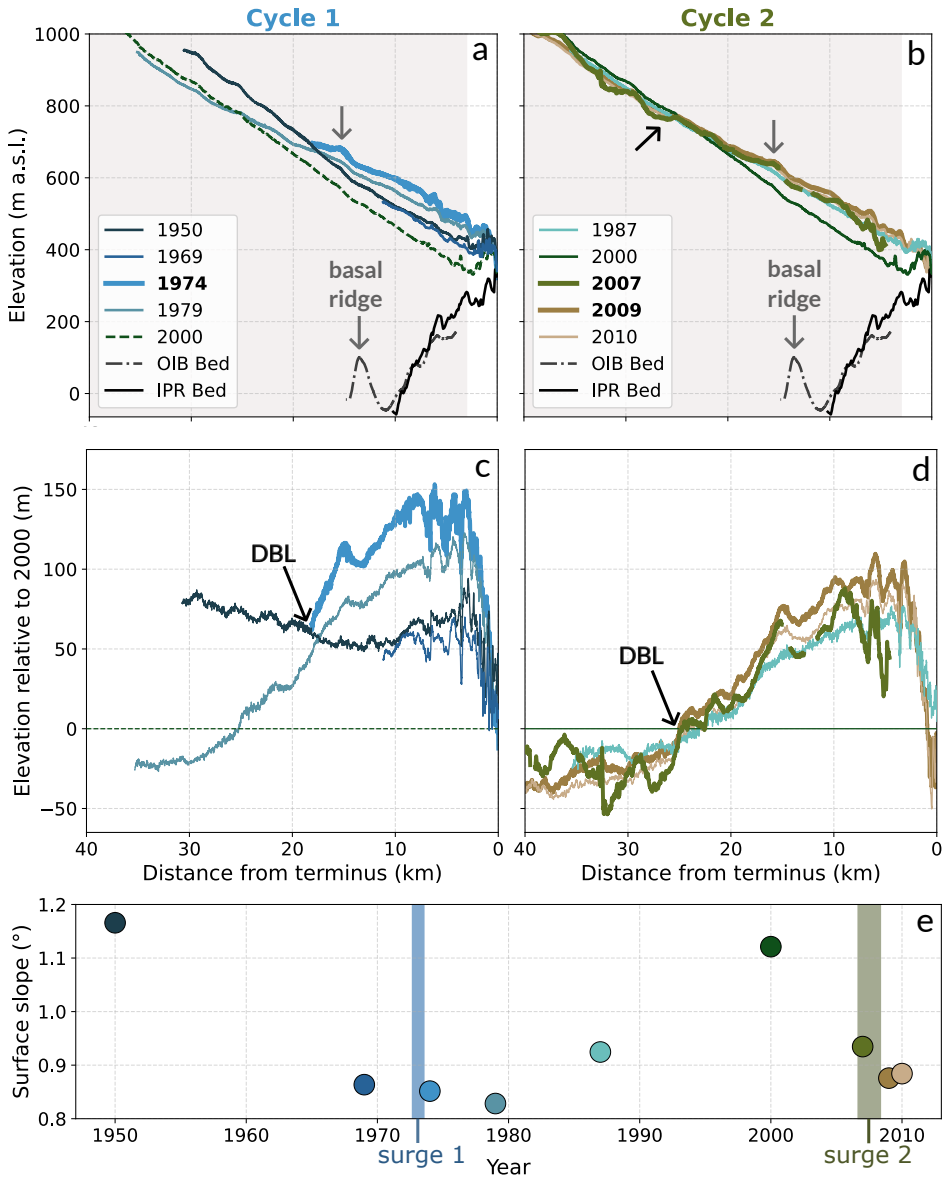


Fig. 3. Evolution of centreline surface profiles of Tweedsmuir Glacier over two surge cycles. The location of the centreline profile is shown in Figure 1. Active surge years are denoted with thick lines and bold text. (a) Absolute elevations during Cycle 1, bracketing the first-observed surge in 1973. (b) Absolute elevations during Cycle 2, bracketing the second-observed surge between 2007 and 2009. The 2000 quiescent profile is shown in both panels for comparison across cycles. Bed topography was acquired from Operation IceBridge (MacGregor and others, 2021) and an unpublished helicopter-basd ice-penetrating radar survey (IPR). Black arrow denotes bumps in the surface topography near the dynamic balance line (hinge point) and grey arrows denote surface bumps that correspond to a basal ridge (discussed in text). (c & d) As per a & b but elevations are relative to the 2000 centreline profile. "DBL" denotes the dynamic balance line. (e) Timeseries of surface slope (relative to horizontal) estimated from a least-squares linear regression of the centreline elevation profiles. The shaded region in panels a and b shows the portion of the surface used in the regression (all but the lower 3 km). The unexpectedly shallow slope in 1969 is likely an artifact of the limited spatial coverage of the DEM (see text).

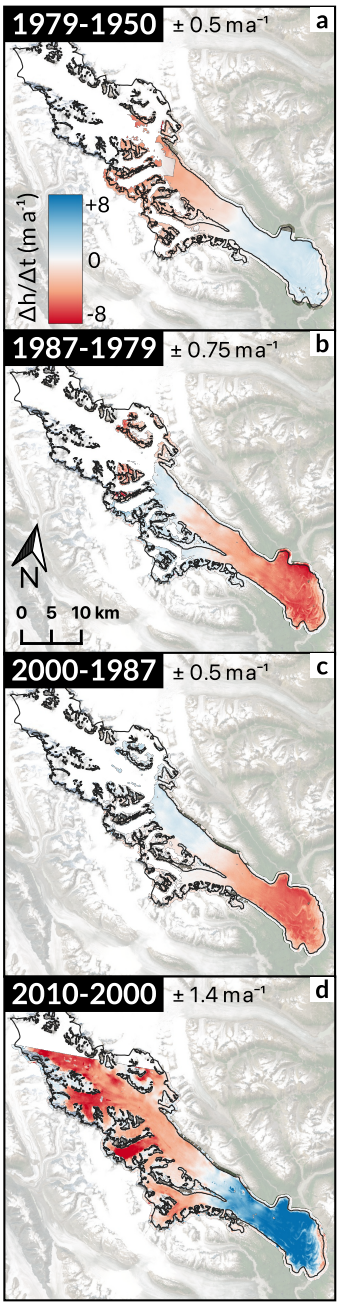


Fig. 4. Rates of elevation (ice thickness) change for a sequence that prioritizes spatial coverage. Mean rates of change reported in the text are calculated within the GLIMS outline (Raup and others, 2007) denoted in black. The vertical uncertainty of each DEM of Difference is printed on each panel as per Equation 3. Surge 1 is captured in panel (a), the following quiescent phase is captured in panels (b) and (c), and Surge 2 is captured in panel (d).

(RGI 7.0 Consortium, 2023) throughout the main trunk, and was manually-adjusted in the terminal lobe to follow more closely to the direction of flow based on a qualitative analysis of the ITS_LIVE (Gardner and others, 2024) multi-year composite velocity vectors (Figure 1, Supplementary Figure S4).

To analyze changes in ice thickness, we created two sequences of DEMs of Difference (DoDs). First, due to the limited spatial coverage of the 1969 and 1974 DEMs (Figure 2), we used the 1950 and 1979 DEMs to bracket Surge 1, producing a sequence with high spatial coverage, including both the receiving zone and most of the reservoir through both surge cycles, but that is limited in temporal resolution (Figure 4). The second DoD sequence prioritizes temporal resolution, but is spatially limited to the receiving zone in the terminus for Surge 1 (Figure 5).

We assume that changes in bed elevations are negligible, as the rates of glacial isostatic uplift in this region are generally on the order of a few centimeters per year (Hu and Freymueller, 2019) and erosion/deposition beneath the glacier is impossible to measure. Annual rates of ice-thickness change ($\Delta h\ \Delta t^{-1}$) are calculated by dividing the change in surface elevation by the number of years in the DoD interval. Maps of the rate of ice thickness change are shown in Figures 4 & 5, and in the text, we report the mean rates of thinning and thickening within the (unbuffered) GLIMS outline. We also assume that most mass transfer occurred during the surge and estimate the corresponding peak rate of ice thickness change for intervals that cover an active surge by dividing the mean change in surface elevation by the number of years elapsed since the surge.

The vertical uncertainty of the DEMs (Table 1) was propagated to the rates of ice-thickness change (Figures 4 & 5) as:

$$\sigma_{\frac{\Delta h}{\Delta t}} = \frac{\sqrt{{\sigma_1}^2 + {\sigma_2}^2}}{\Delta t} \quad (3)$$

where σ_1 and σ_2 are the nMAD for each individual DEM in the DoD pair and Δt is the time between the DEMs.

Terminus position and risk of ice-dam

We manually traced the terminus position of the glacier from orthomosaics produced from the historical images and SPOT5 stereo reconstructions, as described above. Additionally, we traced the terminus in two panchromatic satellite images: one acquired by Landsat7 on 10 August 2000 to match the 2000 SRTM DEM, and one acquired by Landsat9 on 31 August 2025 to provide present-day context.

The terminus of Tweedsmuir Glacier is difficult to map from imagery due to substantial debris-cover, particularly

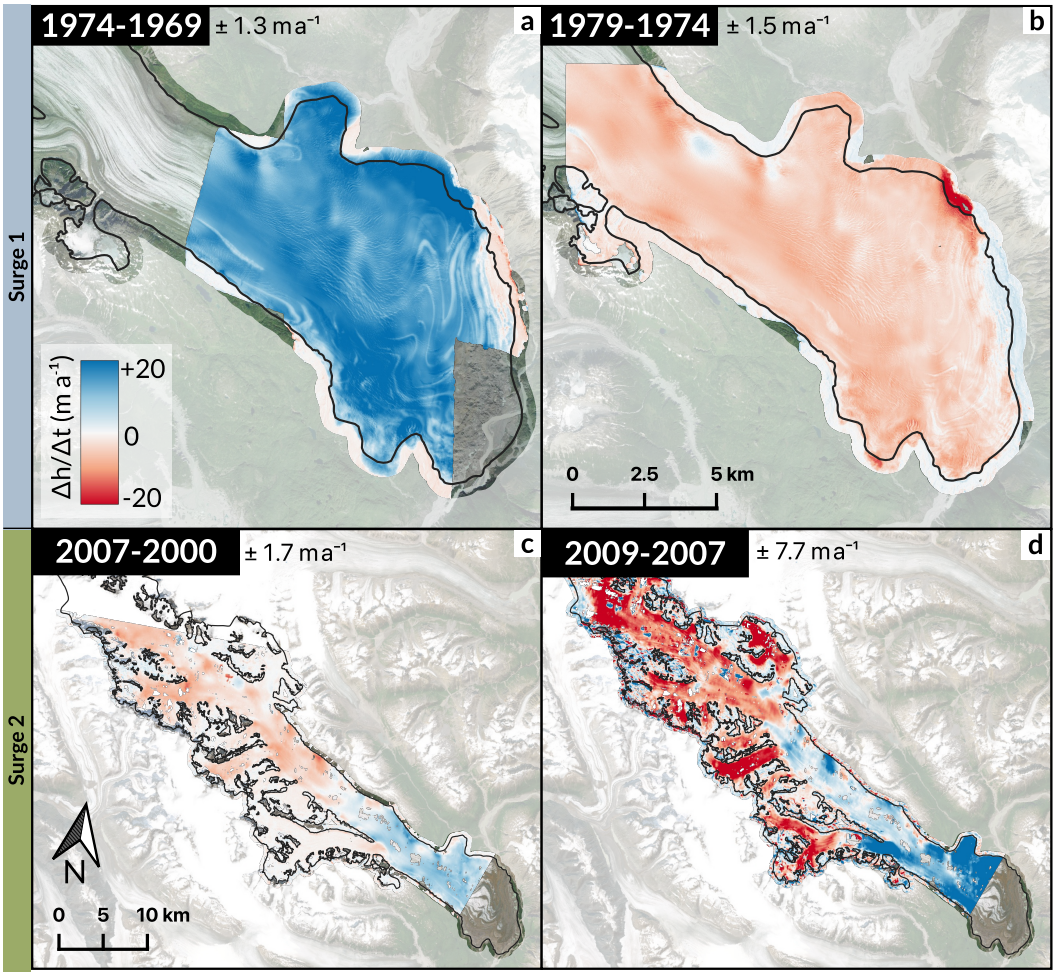


Fig. 5. Rates of elevation (ice thickness) change for a sequence that prioritizes temporal resolution. The vertical uncertainty of each DEM of Difference is printed on each panel as per Equation 3. Top row shows (a) Surge 1 and (b) the first five years of the following quiescent phase. Bottom row shows (c) the beginning of Surge 2 and (d) the rest of the active phase.

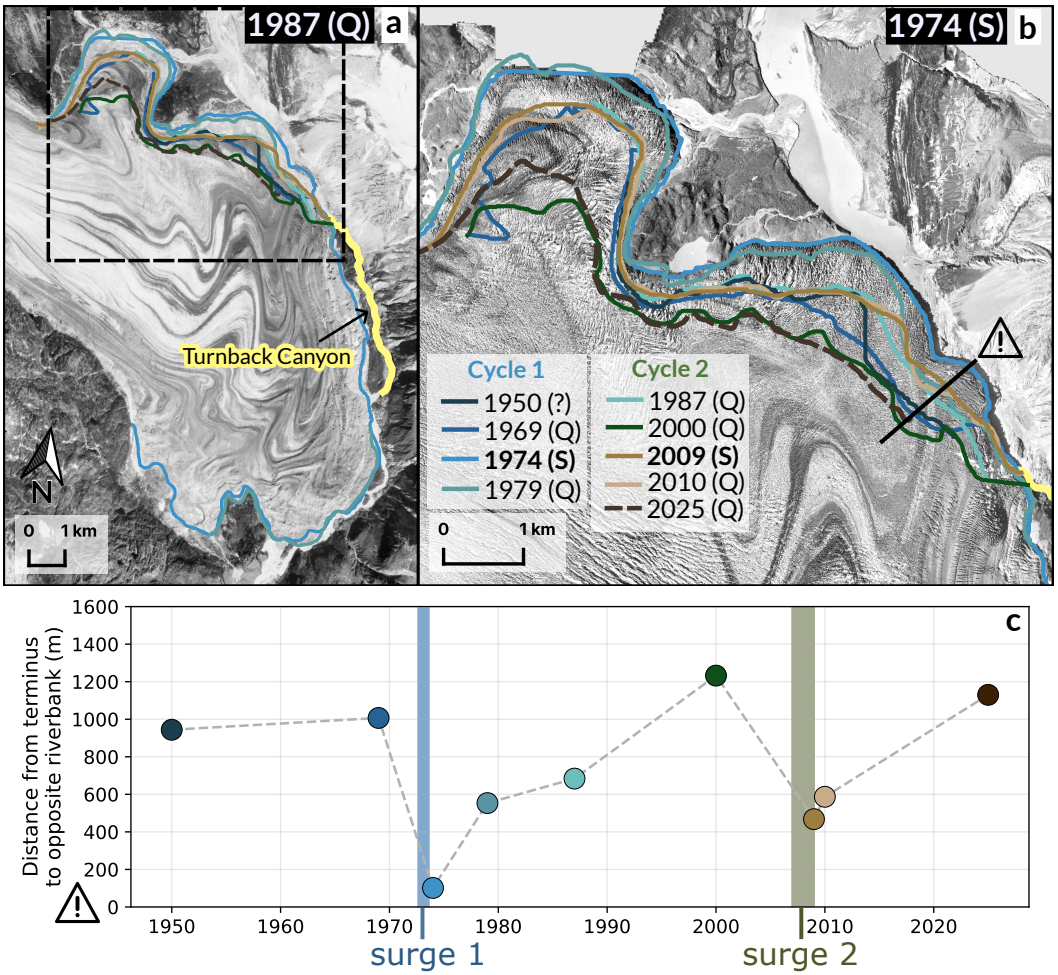


Fig. 6. Potential ice-dam hazard from surges of Tweedsmuir Glacier. Terminus traces are overlaid on orthomoasics from (a) the 1987 quiescent phase and (b) one year after Surge 1. The black dashed box in panel a denotes the extent of panel b, which shows the advance and retreat of the northern portion of the terminus. (c) Distance from the glacier terminus to the riverbank on the opposite side of the Alsek River (denoted by the caution symbol) along the transect in panel b, serving as a proxy for the risk of ice-damming.

the central and southern sections and during quiescent phases (Figure 6 a). We did not attempt to delineate the terminus across debris cover, and therefore, our analysis is confined to the northern section of the terminus (Figure 6 b). The northern section of the terminus is the most variable and hazardous for flooding, as it has historically advanced and contacted the Alsek River during surges (Holdsworth and others, 2002; National Park Service, 2015). The rest of the terminus is less variable as it is restricted by a terminal ridge that confines Turnback Canyon.

As a first-order assessment of the risk of ice damming during surges, we extracted the terminus positions along a transect that extends from the riverbank of the Alsek River on the opposite side of Tweedsmuir Glacier. The transect was manually chosen based on a location in the 1974 post-surge imagery where the glacier extended almost entirely across the river (Figure 6 b). Hence, the "distance from the opposite riverbank" provides a proxy for the risk of an ice dam, assuming a constant configuration of the Alsek River.

Spectral analysis of surface topography

Both theory (Gudmundsson, 2003) and observations (Gudmundsson and others, 2003; De Rydt and others, 2013) suggest that basal topography is transmitted to the glacier surface when the ratio of basal slip to internal deformation is high, such as during surges. In these sliding-dominated regimes, bed undulations with wavelengths of 1–20 ice thicknesses are predicted to appear at the surface, with transfer amplitude peaking at wavelengths of 3–8 ice thicknesses (Figure 8; Gudmundsson, 2003). We therefore expect surface topography in this wavelength range to have greater amplitude during the active surge phase than during quiescence, providing a metric for basal slipperiness throughout the surge cycle. To test this, we quantify surface amplitudes through spectral analysis of the DEM timeseries.

We extracted elevations from each DEM, except for 1969 due to its limited coverage, along three profiles: the centerline profile described in the previous section, together with one additional profile on either side (north and south) of the centerline (Figure 1). The north and south profiles are offset from the centerline by one kilometre in each direction and similarly manually adjusted in the terminal lobe to approximately follow ice flow and therefore target longitudinal undulations in the surface topography, although the velocity field in the terminal lobe is noisy (Supplementary Figure S4). Each profile is sampled every 30 m and detrended with the line of best fit from a least-squares linear regression.

We then performed a Continuous Wavelet Transform (CWT) on each detrended elevation profiles, which decomposes the topographic profile into its frequency content as scaled and shifted versions of a base wavelet function. A notable advantage of the wavelet transform over other spectral transforms, such as traditional implementations of the Fourier transform, is its ability to analyze localized variations in the amplitude spectrum, in this case, along the glacier-surface profiles.

The CWT of a discrete sequence, z_n with length N and sampling interval Δx, is defined as the convolution of z_n with a wavelet function, Ψ (Torrence and Compo, 1998). Therefore, the wavelet amplitude, W_n, is a measure of how well the wavelet, Ψ, matches the sampled topographic profile, z_n:

$$W_n(s) = \sum_{n'=0}^{N-1} z_{n'}\, \Psi^* \left[\frac{(n'-n)\Delta x}{s} \right], \tag{4}$$

where Ψ^* represents the complex conjugate of Ψ. The positional information gained from a wavelet transform is a result of the finite length of the wavelet function (in contrast to the infinite length of a sinusoid in a Fourier transform) as Ψ is scaled by s, and translated along the position index, n (Torrence and Compo, 1998).

We used the popular Morlet wavelet (e.g. Shugar and others, 2010; Ignéczi and others, 2018), a complex sine wave multiplied by a Gaussian envelope (Figure 7 e), to estimate the amplitude of features in the topographic profile. In theory, when using the L_1 normalization, the wavelet amplitude should represent the physical amplitudes of topographic features for undulations shaped similar to the wavelet (Ignéczi and others, 2018; MathWorks, 2021). We report wavelength in units of ice thicknesses, adopting a characteristic ice thickness of $H = 400$ m.

The full amplitude spectra in Figure 7 provide positional context, and the mean spectrum for each profile is compared to theoretical bed-surface transfer amplitudes (Gudmundsson, 2003) in Figure 8. Further, we track the mean amplitude of wavelengths between 3–20 ice thicknesses through time to target features that may be expressions of the underlying bed topography during surges (Figure 9).

RESULTS

Changes in volume and surface slope over 60 years

Surge 1: 1973

Between 1950 and 1979, the reservoir thinned at a mean rate of $-2.3 \pm 0.5\,\mathrm{m\,a^{-1}}$ and the receiving zone thickened at a mean rate of $1.2 \pm 0.5\,\mathrm{m\,a^{-1}}$ (Figure 4 a). Assuming most of the mass transfer occurred during the surge, six years

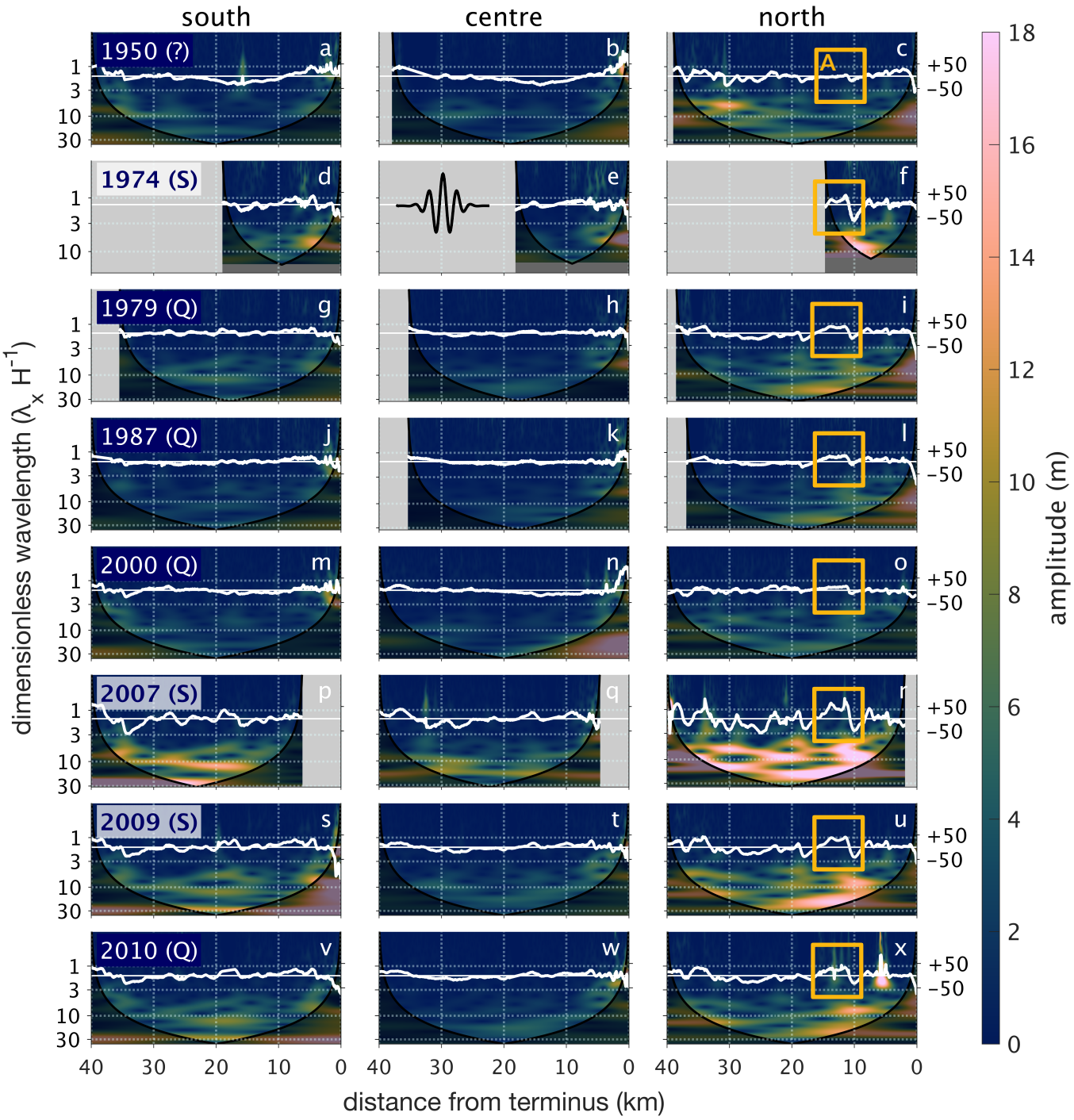


Fig. 7. Continuous Wavelet Transform of detrended glacier surface topography. Locations of the south, centre, and north profiles are shown in Figure 1. Each row represents a year, with the surge phase indicated by S (active surge), Q (quiescence), and ? (unknown). Wavelength is shown in units of ice thicknesses using a characteristic ice thickness of 400 m. The cones of influence (i.e. regions with edge effects) are shaded in black. White lines denote the detrended surface profiles, with amplitude units in metres. Yellow boxes highlight "Feature A" discussed in the text. The Morelet wavelet function is shown in black in panel e.

before the end of the interval, the peak rates of thinning and thickening are $-10.9 \pm 2.3\,\mathrm{m\,a^{-1}}$ and $5.7 \pm 2.3\,\mathrm{m\,a^{-1}}$ in the reservoir and receiving zone, respectively. The terminal lobe thickened at a mean rate of $15.3 \pm 1.3\,\mathrm{m\,a^{-1}}$ between 1969 and 1974 (Figure 5 a).

The dynamic balance line that separates the reservoir from the receiving zone, identified as the line of zero thickness change between 1950 and 1979 (Figure 4 a) and the hinge point between the centreline profiles (Figure 3 c), is located approximately 18 km from the terminus at an elevation of 670 ± 4.8 m a.s.l. We note that although the interval includes six years of change after the surge, the 1974 centreline profile intersects the 1950 profile in a similar location (Figure 3 c), indicating that it is a reasonable approximation.

Along the centreline, the glacier surface is steepest in 1950 and shallows approximately 0.3°, or 25%, by 1969 and 1974 (Figure 3 e). While this is typical following a surge, it is unexpected for the 1969 quiescent profile. Considering only the overlapping sections of the 1950 and 1969 profiles in the lower receiving zone, the slopes and elevations are similar (Figure 3 a,c), with the 1969 profile just 15.6 ± 13.9 m thinner, on average, than in 1950. Thus, the shallow slope in 1969 is likely an artifact of the limited spatial coverage of the DEM.

The terminus position is almost unchanged between 1950 and 1969 (Figure 6). After the surge, the terminus advanced 350 m and 1 km between 1969 and 1974, making contact with the Alsek River (Figure 6 b). The glacier terminus was just 200 m from the opposite riverbank in 1974 (Figure 6 c).

Quiescent Phase: 1974–2007

In the first eight years (1979–1987) of the subsequent quiescent phase, the receiving zone thinned at a mean rate of $-3.5 \pm 0.75\,\mathrm{m\,a^{-1}}$ and the reservoir began to accumulate at a mean rate of $1.2 \pm 0.75\,\mathrm{m\,a^{-1}}$ (Figure 4 b). These rates of change remained comparable, but slightly lower in the following 13 years (1987–2000), with mean rates of thinning and thickening of $-2.8 \pm 0.5\,\mathrm{m\,a^{-1}}$ and $0.9 \pm 0.5\,\mathrm{m\,a^{-1}}$ in the receiving zone and reservoir, respectively (Figure 4 c).

The glacier surface gradually steepened during the quiescent phase, eventually reaching a surface slope in 2000 that is comparable to but slightly shallower than that of 1950 (Figure 3 e). Despite the similarity in surface slope, the glacier was approximately 70 ± 14.2 m thinner in 2000 than in 1950 (Figure 3 c).

The terminus gradually retreated 500 m–1.5 km (depending on the location of measurement) during the quiescent phase, between 1974 and 2000. By 2000, it was 1.4 km from completely covering the Alsek River along the transect in Figure 6.

Surge 2: 2007-2010

Between 2000 and 2007, the receiving zone thickened at a mean rate of $3.7 \pm 1.7\,\mathrm{m\,a^{-1}}$ and the reservoir thinned at a mean rate of $-2.9 \pm 1.7\,\mathrm{m\,a^{-1}}$ (Figure 5 c). However, assuming that most of the mass transfer occurred in the final year of the interval, 2007, the peak rates of thickening and thinning in the receiving zone and reservoir were $25.7 \pm 1.7\,\mathrm{m\,a^{-1}}$ and $-20.3 \pm 1.7\,\mathrm{m\,a^{-1}}$, respectively. In the latter part of the surge, between 2009 and 2010, the receiving zone thickened at $9.6 \pm 7.7\,\mathrm{m\,a^{-1}}$ and the reservoir thinned at $-11.2 \pm 7.7\,\mathrm{m\,a^{-1}}$. The receiving zone extended kilometres further up glacier during this part of the surge than in 2007, and was accompanied by a surge of the southernmost tributary (Figure 5 d).

Ice thickness changes during the 2000–2010 interval (Figure 4 d,) and the hinge point in the centreline profiles (Figure 3 d) show that the dynamic balance line moved up glacier by several kilometres compared to the first-observed surge. During this interval, it is located approximately 23–25 km from the terminus at an elevation of $710 - 730 \pm 5.7$ m a.s.l., 40–70 m higher than during the first surge.

The centreline surface slopes are similar to Surge 1 (Figure 3 e), but the surface elevations are lower during this cycle. This is apparent in the 2007, 2009, and 2010 active- and post-surge profiles, which are approximately 50 m lower than the 1974 post-surge surface (Figure 3 c,d). The ice thickness during and after Surge 2 is instead comparable to that of 1987, approximately halfway through the preceding quiescent phase (Figure 3 d).

Similarly, terminus positions for comparable surge phases have retreated between the two cycles, extending only as far after the surge in 2009 as the 1987 quiescent-phase terminus, or 250–700 m further upstream than the 1974 post-surge extent (Figure 6 b). The terminus was 600 m from reaching the riverbank on the opposite side of the Alsek river after Surge 2 (Figure 6 c).

Amplification of surface topography during surges

A consistent pattern in the CWT spectra is the amplification of surface features ("bumps") with wavelengths greater than three ice thicknesses during surges, compared to quiescent phases (Figures 7, 8, & 9). This is most apparent in the northern profile, but the cycle is captured in all profiles by our new metric: the average amplitude of the 3–20 ice thickness wavelengths (Figure 9). Although the centreline profiles have substantially lower amplitudes than the northern and southern profiles, the same pattern persists, with amplitudes

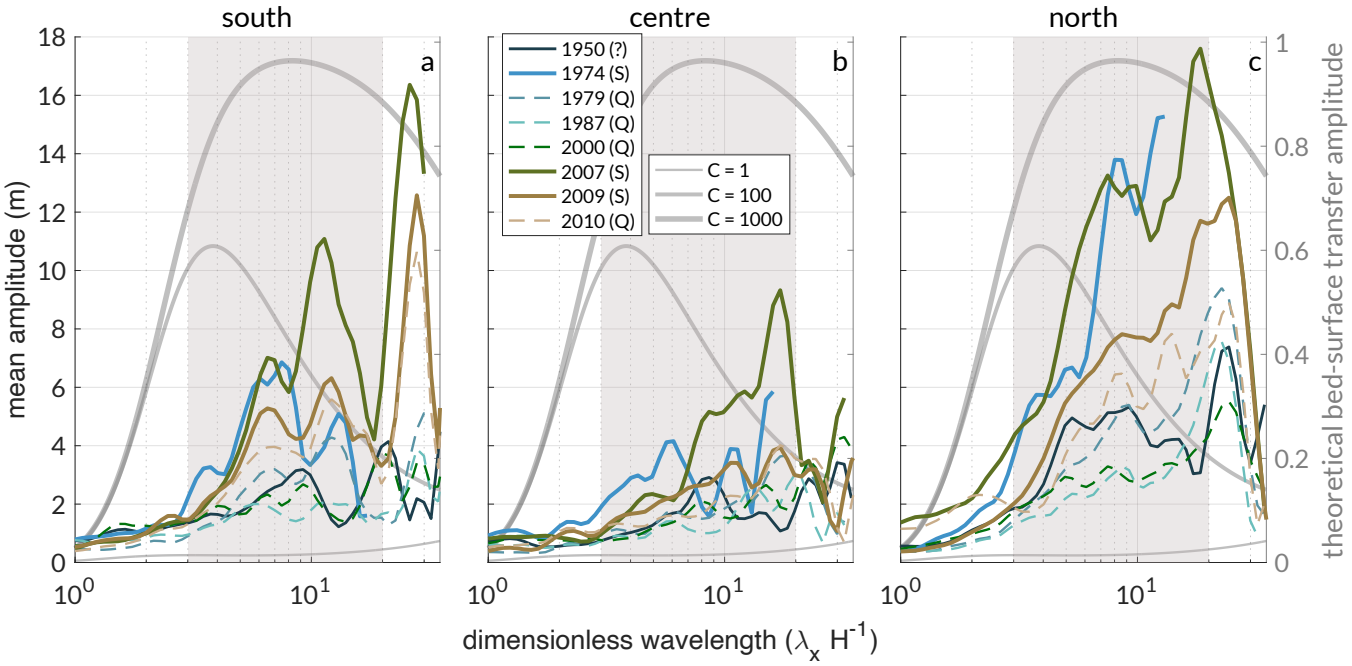


Fig. 8. Mean wavelet amplitudes of each wavelength in the surface profiles. Surge years are denoted by bold solid lines, quiescence by dashed lines, and the unknown phase (1950) by a thin solid line. The grey line (right axis) is the theoretical steady-state amplitude of a surface undulation caused by an underlying bed undulation for a slippery bed, expressed as the ratio of the surface and bed undulation amplitudes (equation 75 in Gudmundsson (2003) with slip ratios C = 1, 100, 1000 and surface slope = 0.003 radians, as in Figure 1 of De Rydt and others (2013)). Shaded region is the range of the wavelengths averaged for the amplitude metric in Figure 9 (3–20 ice thicknesses, assuming a characteristic wavelength of 400 m).

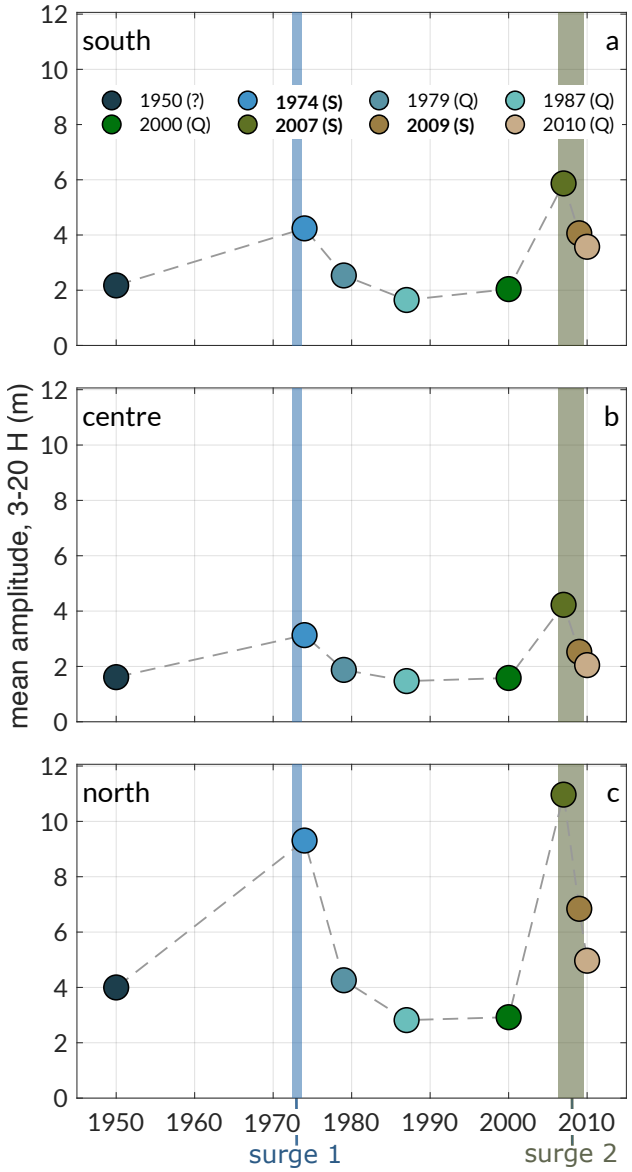


Fig. 9. Mean wavelet amplitudes of wavelengths between 3–20 ice thicknesses for each surface profile (shaded region in Figure 8), assuming a characteristic wavelength of 400 m.

consistently greater in surge phases than quiescent phases (Figure 8).

The glacier surface in 1950, a previously-undocumented phase of the surge cycle, has similar spectral characteristics to the known quiescent phases. It has lower amplitudes than the surge surfaces across all profiles (Figure 7, Figure 9) and all wavelengths (Figure 8), but is particularly bumpy in the upper half of the northern profile with wavelengths of 5–9 ice thicknesses (Figure 7 c). Similarly, the mean amplitude of wavelengths within the target 3–20 ice thickness band in 1950 is 1.5–2.5 times lower than following Surge 1 (Figure 9).

Some surface bumps persist throughout all phases, but their amplitudes decay with time following surges. For example, "Feature A" in Figure 7 (yellow box) decays from a wavelet amplitude of approximately 18 m immediately after Surge 1 (1974) to 8–10 m just six years after the surge (1979), and again from 22 m during Surge 2 (2007) to 12–14 m immediately following the surge (2009 and 2010, respectively).

We find that the wavelet amplitudes are notably smaller than the physical amplitudes in the elevation profiles. For example, "Feature A" has a true amplitude of approximately 50 m in 2007 but a wavelet amplitude of 22 m (Figure 7 r). Because the CWT is a correlation between the signal and the scaled Morlet wavelet (illustrated in Figure 7 e), the wavelet amplitude reflects the degree of similarity between a given topographic feature and the wavelet's characteristic shape at a given scale (Equation 4). For features whose shape differs from the shape of the wavelet, energy is distributed across a range of scales rather than concentrated at the scale corresponding to the feature's true wavelength, and therefore peak wavelet amplitude typically underestimates the feature's actual amplitude. Thus, we find that wavelet amplitude is a robust measure of *relative* feature strength across scales, rather than an absolute measure of physical relief.

DISCUSSION

Evolution of surge behaviour over six decades

Our dataset extends beyond the previously documented observational record, leaving the surge phase of Tweedsmuir Glacier in 1950 unknown. Determining the phase represented by 1950 is important for assessing changes in surge-cycle length and magnitude through time. We therefore first combine observational proxies to infer the most likely surge phase represented by the 1950 DEM and then consider how the glacier has evolved across surge cycles.

Inferences and implications of the phase of 1950

Without any accounts of surges of Tweedsmuir Glacier prior to 1973, we rely on proxies to determine the glacier's position within the surge cycle in 1950. We compiled three standard metrics: ice thickness, surface slope, and terminus position (all relative to known surge phases), and a new metric: the amplitude of surface topography. We are confident that the glacier is in a quiescent phase in 1950 due to its thin receiving zone (Figure 3 a; Figure 4 a), steep slope (Figure 3 e), retreated surface position (Figure 6), and smooth surface topography relative to the active- and post-surge phases (Figure 9).

Further, we suggest that 1950 represents the middle to end of a quiescent phase. First, the steep slope of the 1950 centreline, particularly in the reservoir, is comparable to—and actually greater than—that of 2000, 80% through the quiescent phase in Cycle 2 (Figure 3 a,c). Similarly, the amplitude of "Feature A" in Figure 7 (yellow box), which is consistently amplified during surges and subsequently decays throughout quiescence, is almost non-existent in 1950 (Figure 7 c), similar to the 2000 profile (Figure 7 o). Next, the ice thickness in the receiving zone is essentially unchanged between 1950 and 1969 (Figure 3 a). We would expect significant surface lowering in the receiving zone over 19 years of a quiescent phase, as is observed over the 13 years between 1987 and 2000 (Figure 3 b). Finally, the terminus position is also almost unchanged between 1950 and 1969 (Figure 6). Again, we would expect a greater retreat over two decades of a quiescent phase.

Taken together, these four proxies suggest that the glacier was approaching the end of a quiescent phase in 1950 and that there may have been an undocumented surge between 1950 and 1969, implying a cycle length of less than 22 years (1951–1973), substantially shorter than the 34-year cycle captured in this study (1973–2007). As an additional line of evidence, we note the kilometre-scale advance and compression of medial moraines in the terminus between 1950 and 1969 (Figure 10 b), typical of surges (Figure 10 c, e.g. Post, 1972; Young and others, 2022), compared to virtually no change during known quiescent phases (Figure 10 d).

However, without direct observations, we cannot rule out an alternative interpretation: that there was *not* a surge between 1950 and 1969 and that the cycle length remained constant at 34 years, placing the previous surge in the early 1940s. This alternative requires unexpectedly low rates of thinning in the receiving zone and terminus retreat during the last 70% of the quiescent phase (1950–1973). It also requires that the glacier sustained a driving stress exceeding that at which Surge 2 initiated for 23 years (1950–1973) without surging (Figure 3). Both interpretations therefore imply a change in surge behaviour through time. If a surge occurred between 1950 and 1969, the surge cycle has lengthened. If it did not, the threshold driving stress at which surges are triggered has decreased.

Climatic controls on surge behaviour

The suite of observations presented in this study suggests that between comparable surge phases, the glacier thinned and the terminus retreated through time, the dynamic balance line moved upstream, and the cycle lengthened and/or the two surges initiated at different driving stresses. Individually, each of these metrics are controlled by surge dynamics, but collectively, they indicate a climatically-driven change in surge behaviour with the current trend of warming and negative mass balance across Alaskan and Yukon glaciers (e.g. Larsen and others, 2015; Wells and others, 2026).

Thinning (Figure 3) and terminus retreat (Figure 6) between the two surge cycles indicate that the rate of ablation exceeds the replenishment from surges in the lower ablation zone, and the terminus may continue to retreat on timescales greater than the length of the surge cycle. Additionally, if 1950 represents a late-stage quiescent phase and an undocumented surge occurred shortly thereafter, the resulting surge cycle would have lasted less than 22 years (1951–1973), substantially shorter than the 34-year cycle captured in this study (1973–2007). A lengthening of the surge cycle is consistent with a negative mass balance, as a lower accumulation rate leading up to a surge can increase the time it takes to build up sufficient driving stress to initiate a surge (Eisen and others, 2001).

The dynamic balance line moved approximately 5 km upglacier over the study period (Figure 3, Figure 4). Although our observations suggest that the 1950 DEM might represent a different surge cycle than the 1973 DEM, the 1950 and 1979 observations provide a benchmark for the position of the dynamic balance line during the 1–2 cycles preceding the 2007–2009 surge. By definition, the dynamic balance line is the downstream limit of the reservoir zone that accumulates mass leading up to a surge. The factors controlling its position on a given glacier are not well understood but have been observationally linked to bedrock ridges (Flowers and others, 2011; Liu and others, 2024). We note a prominent ridge in the Operation IceBridge bed profile and a consistent surface bump just downstream of the dynamic balance line in Surge 1 (grey arrow in Figure 3 a), and another particularly bumpy portion of the surface in the same locations as the dynamic balance line in Surge 2 (black arrow in Figure 3 b). Thus, it is possible that the dynamic balance line on Tweedsmuir Glacier aligns with basal ridges and has migrated upstream in response to glacier thinning. However,

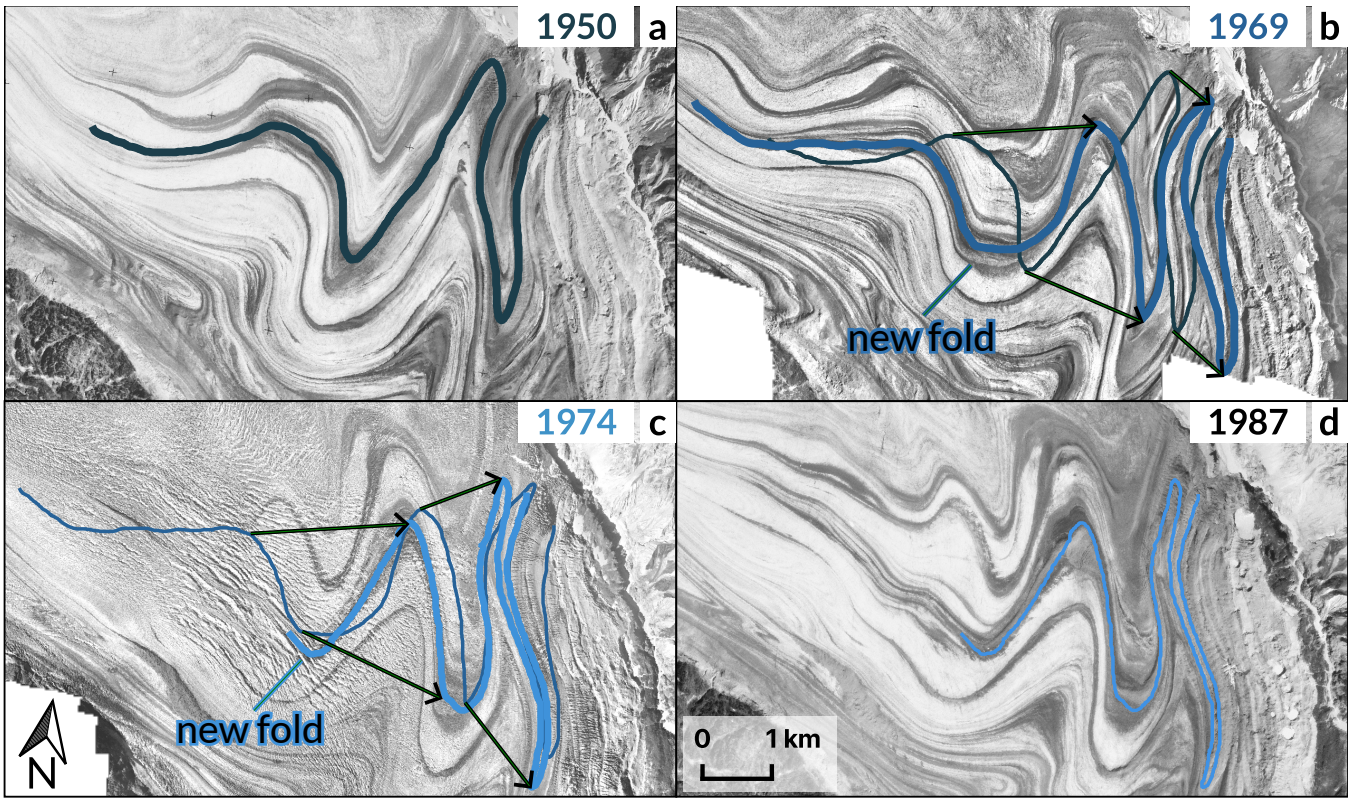


Fig. 10. Advance and compression of medial moraines between 1950 and 1969 (a & b) and following the known surge in 1973 (c). Moraines are almost unchanged during quiescence (d). Manually-traced moraines are overlaid on orthomosaics from historical air photos for each respective year, with the previous orthomosaic trace provided for reference as a thin line. Arrows indicate displacement of moraine folds. Successive moraine traces are indistinguishable during quiescence, so only the 1974 trace is overlaid on panel d.

without observations of the bed, this idea remains speculative.

While surges may become less expansive and/or less frequent in the future, the dynamic balance line remains in the ablation area (Figures 3, 4, & 5), tens of kilometres below the end-of-summer snowline in our image sets (Figure 2)—another line of evidence that its position is dynamically controlled rather than climatically controlled. In addition, Surge 2 was able to initiate with a lower driving stress (constant or lower α, lower H) than Surge 1. Thus, dynamic refilling of the reservoir still outpaces climatic mass loss in the upper ablation zone and we expect surges of Tweedsmuir Glacier to continue in the future.

Diminishing threat of ice dams and implications for the Alsek River

The northern portion of the terminal lobe, upstream of Turnback Canyon, poses the greatest risk of an ice-dam across the Alsek River, as the rest of the terminus is confined by a bedrock ridge. Our results suggest that this is a diminishing hazard (neglecting potential re-configurations of the river), as the most recent, 2009–2010, post-surge terminus was several-hundred-metres less extensive than in 1973 (Figure 6). Given the position of the glacier at the time of writing (2025), the terminus would be required to advance at least 1.2 km during the next surge to reach the opposite side of the river (Figure 6 c)—an advance even greater than that of the 1973 surge, which is unlikely given the observations in this study and the negative mass balance across Alaska and the Yukon (e.g. Larsen and others, 2015; Wells and others, 2026).

An interesting question is how the Alsek River will respond to the retreating terminus of Tweedsmuir Glacier. If the northern portion of the terminus continues to retreat at a rate of 400 m per surge cycle (Figure 6) and assuming a constant cycle length 34 years (likely a minimum-bound), the terminus of Tweedsmuir Glacier could retreat over 3 km by 2300. Thus, the Alsek River could occupy a new route in the next few centuries and possibly bypass Turnback Canyon. However, a re-configuration of the river would need to erode substantial material at and beneath the present-day terminus of Tweedsmuir Glacier. Our results constrain the temporal and spatial patterns of retreat for further geomorphological studies that would be required to answer this question.

Insights on improved inversions of bed topography

It has been proposed that surges can be leveraged to improve bed inversions (Morin and others, 2023), since basal topography with wavelengths of 1–20 ice thicknesses are transmitted to the surface in high-slip regimes (Gudmundsson, 2003; Gudmundsson and others, 2003; De Rydt and others, 2013). Although we lack sufficient basal topographic data to directly test this hypothesis, it is likely that the surface bumps amplified during surges on Tweedsmuir Glacier reflect corresponding features in the bed. With spectral analysis, we show that these bumps begin to decay immediately following a surge. Thus, under this assumption, a "bed-representative" surface persists for only one year following the active surge at Tweedsmuir Glacier. While this timescale should be calibrated with other surge-type glaciers, our observations suggest that to truly leverage the high-slip regime, bed inversions should use surface topography acquired during or immediately following a surge. With new tools such as HSfM (Knuth and others, 2023), surface topography can be reconstructed from historical images and combined with modern surge observations to improve spatiotemporal data coverage and increase signal-to-noise ratios. This study serves as a framework for such opportunities.

CONCLUSION

Improving the observational record of surge dynamics is particularly important for understanding how glaciers in the Saint Elias Mountains will interact with their surrounding landscapes and ecosystems in the future. Advances in remote-sensing techniques over the past decade have created new opportunities to analyze long-term changes of surge-type glaciers with cycles that are multiple decades long. In this study, we extend the surge record of Tweedsmuir Glacier back to 1950 using multi-temporal Structure from Motion photogrammetry with historical aerial photographs. We show that across two surge cycles, the glacier has thinned, the terminus has retreated, and the dynamic balance line has moved a few kilometres upstream. Collectively, these characteristics, along with surface slope and a new metric: the amplification of surface topography, indicate a corresponding change in either surge-cycle length or the threshold driving stress at which surges of Tweedsmuir Glacier initiate. While surges of Tweedsmuir Glacier will continue in the future, continued retreat of the terminus may diminish the historically-prevalent hazard of an ice dam across the Alsek River (in its current configuration). This study provides a framework for tracking the multidecadal evolution of surge-type glaciers using observable surface signatures of surges, and offers new insight for improving inversions of the bed topography beneath them.

ACKNOWLEDGEMENTS

This research was funded through National Sciences and Engineering Council of Canada (NSERC) Discovery Grant and Discovery Accelerator Supplements 2020-04207, Alpine Club of Canada Environment Grant, University of Calgary teaching assistant support, and fieldwork supported by BC Park permit number 109728. We extended our gratitude to the Research and Academic Computing Services (RACS) team in the College of Earth, Ocean, and Atmospheric Sciences at Oregon State University for their support with the computational resources used for image processing. We thank Laurent Mingo (Blue System Integration, Ltd.) for contributions to radar data collection and interpretation, and Gryphen Goss for her contribution of ideas and thoughtful discussions throughout this project. We acknowledge that we are visitors to Tweedsmuir Glacier and the traditional territories of the Champagne and Aishihik First Nations.

AUTHOR CONTRIBUTIONS

DHS, GEF, and MAS developed the project idea and objectives. MAS led the analysis and writing of the paper, including the creation of figures. All co-authors provided mentorship and expertise of scientific concepts and contributed to manuscript editing. MAS produced the historical DEMs and orthomosaics with mentorship provided by DHS and FK, and performed the wavelet transform. AF produced the satellite-derived DEMs and orthomosaics. DHS and GEF collected the unpublished ice-penetrating radar, which was processed by GEF.

DATA AVAILABILITY

All Digital Elevation Models, Orthomosaics, and metadata used for HSfM processing will be publicly available with a doi on Zenodo after peer-review. Both historical image pre-processing (HIPP) and historical Structure from Motion (HSfM) are open-source and available at Knuth and others (2021) and Knuth and others (2023). Landsat images can be downloaded from USGS Earth Explorer.

AI DECLARATION

Artificial Intelligence (AI) and AI-assisted technologies were used during the research processes to debug code, specifically to produce author-defined figure layouts and aesthetics using ChatGPT and Claude Sonnet 5. In the writing process, ChatGPT and Grammarly were used to assist with grammar, spelling, and sentence structure. AI was not used to generate ideas, analyze or extract insights from data, nor to generate original text or images for this paper.

REFERENCES

Agisoft Metashape (2023) 2.0.3 Professional Edition

Benn DI, Fowler AC, Hewitt I and Sevestre H (2019) A general theory of glacier surges. *Journal of Glaciology*, **65**(253), 701–716, ISSN 0022-1430 (doi: 10.1017/jog.2019.62)

Bevington A and Copland L (2014) Characteristics of the last five surges of Lowell Glacier, Yukon, Canada, since 1948. *Journal of Glaciology*, **60**(219), 113–123, ISSN 1727-5652 (doi: 10.3189/2014JoG13J134)

Beyer RA, Alexandrov O and McMichael S (2018) The Ames Stereo Pipeline: NASA's Open Source Software for Deriving and Processing Terrain Data. *Earth and Space Science*, **5**(9), 537–548, ISSN 2333-5084 (doi: 10.1029/2018EA000409)

Bhambri R, Hewitt K, Kawishwar P, Kumar A, Verma A, Snehmani, Tiwari S and Misra A (2019) Ice-dams, outburst floods, and movement heterogeneity of glaciers, Karakoram. *Global and Planetary Change*, **180**, 100–116, ISSN 0921-8181 (doi: 10.1016/j.gloplacha.2019.05.004)

Björnsson H (1998) Hydrological characteristics of the drainage system beneath a surging glacier. *Nature*, **395**(6704), 771–774, ISSN 1476-4687 (doi: 10.1038/27384)

Champagne & Ashihik First Nations (2006) Climate Change in our backyard. In *Climate Change in Our Backyard*, Haines Junction

Clague J and Rampton V (2011) Neoglacial Lake Alsek. *Canadian Journal of Earth Sciences*, **19**, 94–117 (doi: 10.1139/e82-008)

Clarke GKC, Collins SG and Thompson DE (1984) Flow, thermal structure, and subglacial conditions of a surge-type glacier. *Canadian Journal of Earth Sciences*, **21**(2), 232–240, ISSN 0008-4077, 1480-3313 (doi: 10.1139/e84-024)

Crompton JW, Flowers GE and Stead D (2018) Bedrock Fracture Characteristics as a Possible Control on the Distribution of Surge-Type Glaciers. *Journal of Geophysical Research: Earth Surface*, **123**(5), 853–873, ISSN 2169-9011 (doi: 10.1002/2017JF004505)

Cuffey K and Paterson WSB (2010) *The Physics of Glaciers*. Book, Whole, Academic Press, Burlington, MA, 4 edition, ISBN 0123694612;9780123694614;

Dawson N, Fischer J, Kuhn M, Pasotti A, mhugent, Rouzaud D, Sutton T, Bruy A, Dobias M, Pellerin M, Rouault E, Olaya V, Blottiere P, Macho W, Blazek R, Sherman G, Sant-anna H, Woodrow N, Bartoletti L, Cabieces J, rldhont, signedav, Shaffer L, Belgacem N, Santilli S, Natsis S, Larosa S, Mani S, Cloarec V and Jurgiel B (2025) Qgis/QGIS: 3.34.15. Zenodo (doi: 10.5281/zenodo.14678619)

De Paoli L and Flowers GE (2009) Dynamics of a small surge-type glacier using one-dimensional geophysical inversion. *Journal of Glaciology*, **55**(194), 1101–1112, ISSN 0022-1430 (doi: 10.3189/002214309790794850)

De Rydt J, Gudmundsson GH, Corr HFJ and Christoffersen P (2013) Surface undulations of Antarctic ice streams tightly controlled by bedrock topography. *The Cryosphere*, **7**(2), 407–417 (doi: 10.5194/tc-7-407-2013)

Dowdeswell JA, Hamilton GS and Hagen JO (1991) The duration of the active phase on surge-type glaciers: Contrasts between Svalbard and other regions. *Journal of Glaciology*, **37**(127), 388–400, ISSN 0022-1430, 1727-5652 (doi: 10.3189/S0022143000005827)

Dowdeswell JA, Hodgkins R, Nuttall AM, Hagen JO and Hamilton GS (1995) Mass balance change as a control on the frequency and occurrence of glacier surges in Svalbard, Norwegian High Arctic. *Geophysical Research Letters*, **22**(21), 2909–2912, ISSN 0094-8276 (doi: 10.1029/95GL02821)

Doyle SH, Hubbard B, Christoffersen P, Young TJ, Hofstede C, Bougamont M, Box JE and Hubbard A (2018) Physical Conditions of Fast Glacier Flow: 1. Measurements From Boreholes Drilled to the Bed of Store Glacier, West Greenland. *Journal of Geophysical Research: Earth Surface*, **123**(2), 324–348, ISSN 2169-9003 (doi: 10.1002/2017JF004529)

Eisen O, Harrison WD and Raymond CF (2001) The surges of Variegated Glacier, Alaska, U.S.A., and their connection to climate and mass balance. *Journal of Glaciology*, **47**(158), 351–358, ISSN 0022-1430, 1727-5652 (doi: 10.3189/172756501781832179)

Eisen O, Harrison WD, Raymond CF, Echelmeyer KA, Bender GA and Gorda JL (2005) Variegated Glacier, Alaska, USA: A century of surges. *Journal of Glaciology*, **51**(174), 399–406, ISSN 0022-1430, 1727-5652 (doi: 10.3189/172756505781829250)

Facciolo G, Franchis CD and Meinhardt E (2015) MGM: A Significantly More Global Matching for Stereovision. In *Procedings of the British Machine Vision Conference 2015*, 90.1–90.12, British Machine Vision Association, Swansea, ISBN 978-1-901725-53-7 (doi: 10.5244/C.29.90)

Flowers GE, Roux N, Pimentel S and Schoof CG (2011) Present dynamics and future prognosis of a slowly surging glacier. *The Cryosphere*, **5**(1), 299–313, ISSN 1994-0416 (doi: 10.5194/tc-5-299-2011)

Fowler AC, Murray T and Ng FSL (2001) Thermally controlled glacier surging. *Journal of Glaciology*, **47**(159), 527–538, ISSN 0022-1430, 1727-5652 (doi: 10.3189/172756501781831792)

Frappé TP and Clarke GKC (2007) Slow surge of Trapridge Glacier, Yukon Territory, Canada. *Journal of Geophysical Research: Earth Surface*, **112**(F3), ISSN 0148-0227 (doi: 10.1029/2006JF000607)

Gardner A, Fahnestock M, Greene C, Kennedy J, Liukis M, Lopez L and Scambos T (2024) MEASURES ITS_LIVE Regional Glacier and Ice Sheet Surface Velocities, Version 2 (doi: 10.5067/JQ6337239C96)

Gudmundsson GH (2003) Transmission of basal variability to a glacier surface. *Journal of Geophysical Research: Solid Earth*, **108**(B5), ISSN 0148-0227 (doi: 10.1029/2002JB002107)

Gudmundsson GH, Aðalgeirsdóttir G and Björnsson H (2003) Observational verification of predicted increase in bedrock-to-surface amplitude transfer during a glacier surge. *Annals of Glaciology*, **36**, 91–96, ISSN 0260-3055, 1727-5644 (doi: 10.3189/172756403781816248)

Hewitt K and Liu J (2010) Ice-Dammed Lakes and Outburst Floods, Karakoram Himalaya: Historical Perspectives on Emerging Threats. *Physical Geography*, **31**(6), 528–551, ISSN 0272-3646 (doi: 10.2747/0272-3646.31.6.528)

Hirschmuller H (2008) Stereo Processing by Semiglobal Matching and Mutual Information. *IEEE Transactions on Pattern Analysis and Machine Intelligence*, **30**(2), 328–341, ISSN 1939-3539 (doi: 10.1109/TPAMI.2007.1166)

Höhle J and Höhle M (2009) Accuracy assessment of digital elevation models by means of robust statistical methods. *ISPRS Journal of Photogrammetry and Remote Sensing*, **64**(4), 398–406, ISSN 0924-2716 (doi: 10.1016/j.isprsjprs.2009.02.003)

Holdsworth G, Howarth PJ and Ommanney SLC (2002) Quantitative Measurements of Tweedsmuir Glacier and Lowell Glacier Imagery. In *Glaciers of North America- GLACIERS OF CANADA*, Satellite Image Atlas of Glaciers of the World: Glaciers of North America–Glaciers of Canada. (USGS Professional Paper 1386-J), J312–J324, US Geological Survey, Reston, VA,

Hu Y and Freymueller JT (2019) Geodetic Observations of Time-Variable Glacial Isostatic Adjustment in Southeast Alaska and Its Implications for Earth Rheology. *Journal of Geophysical Research: Solid Earth*, **124**(9), 9870–9889, ISSN 2169-9356 (doi: 10.1029/2018JB017028)

Ignéczi Á, Sole AJ, Livingstone SJ, Ng FSL and Yang K (2018) Greenland Ice Sheet surface topography and drainage structure controlled by the transfer of basal variability. *Frontiers in Earth Science*, **6**, 101, ISSN 2296-6463 (doi: 10.3389/feart.2018.00101)

Kamb B, Raymond CF, Harrison WD, Engelhardt H, Echelmeyer KA, Humphrey N, Brugman MM and Pfeffer T (1985) Glacier surge mechanism: 1982-1983 surge of Variegated Glacier, Alaska. *Science*, **227**(4686), 469–479 (doi: 10.1126/science.227.4686.469)

Knuth F, Schwat E, Shean D and McNeil C (2021) Historical Image Pre-Processing (HIPP) pre-release v0.1. Zenodo (doi: 10.5281/zenodo.5510876)

Knuth F, Shean D, Bhushan S, Schwat E, Alexandrov O, McNeil C, Dehecq A, Florentine C and O'Neel S (2023) Historical Structure from Motion (HSfM): Automated processing of historical aerial photographs for long-term topographic change analysis. *Remote Sensing of Environment*, **285**, 113379, ISSN 0034-4257 (doi: 10.1016/j.rse.2022.113379)

Kochtitzky W, Jiskoot H, Copland L, Enderlin E, Mcnabb R, Kreutz K and Main B (2019) Terminus advance, kinematics and mass redistribution during eight surges of Donjek Glacier, St. Elias Range, Canada, 1935 to 2016. *Journal of Glaciology*, **65**(252), 565–579, ISSN 0022-1430, 1727-5652 (doi: 10.1017/jog.2019.34)

Kochtitzky W, Winski D, McConnell E, Kreutz K, Campbell S, Enderlin EM, Copland L, Williamson S, Main B and Jiskoot H (2020) Climate and surging of Donjek Glacier, Yukon, Canada. *Arctic, Antarctic, and Alpine Research*, **52**(1), 264–280, ISSN 1523-0430 (doi: 10.1080/15230430.2020.1744397)

Korona J, Berthier E, Bernard M, Rémy F and Thouvenot E (2009) SPIRIT. SPOT 5 stereoscopic survey of Polar Ice: Reference Images and Topographies during the fourth International Polar Year (2007–2009). *ISPRS Journal of Photogrammetry and Remote Sensing*, **64**(2), 204–212, ISSN 0924-2716 (doi: 10.1016/j.isprsjprs.2008.10.005)

Krimmel R and Meier M (1975) Glacier applications of ERTS images. *Journal of Glaciology*, **15**(73), 391–401, ISSN 0022-1430 (doi: 10.1017/S002214300003450X)

Larsen CF, Burgess E, Arendt AA, O'Neel S, Johnson AJ and Kienholz C (2015) Surface melt dominates Alaska glacier mass balance. *Geophysical Research Letters*, **42**(14), 5902–5908, ISSN 1944-8007 (doi: 10.1002/2015GL064349)

Lindsey CC (1975) Proglacial lakes and fish dispersal in southwestern Yukon Territory. *SIL Proceedings, 1922-2010*, **19**(3), 2364–2370, ISSN 0368-0770 (doi: 10.1080/03680770.1974.11896319)

Liu J, Enderlin EM, Bartholomaus TC, Terleth Y, Mikesell TD and Beaud F (2024) Propagating speedups during quiescence escalate to the 2020–2021 surge of Sít' Kusá, southeast Alaska. *Journal of Glaciology*, **70**, e57, ISSN 0022-1430, 1727-5652 (doi: 10.1017/jog.2023.99)

Lovell AM, Carr JR and Stokes CR (2018) Topographic controls on the surging behaviour of Sabche Glacier, Nepal (1967 to 2017). *Remote Sensing of Environment*, **210**, 434–443, ISSN 0034-4257 (doi: 10.1016/j.rse.2018.03.036)

Lovell H, Benn DI, Jiskoot H, Stokes CR, Flowers GE, Guillet G, Mannerfelt ES, Falaschi D, Kääb A, King O, Benediktsson ÍÖ, Bhambri R, Lv M, Muhammad S and Luckman A (2026) Glacier surging and surge-related hazards in a changing climate. *Nature Reviews Earth & Environment*, **7**(3), 162–180, ISSN 2662-138X (doi: 10.1038/s43017-025-00757-9)

MacGregor JA, Boisvert LN, Medley B, Petty AA, Harbeck JP, Bell RE, Blair JB, Blanchard-Wrigglesworth E, Buckley EM, Christoffersen MS, Cochran JR, Csathó BM, De Marco EL, Dominguez RT, Fahnestock MA, Farrell SL, Gogineni SP, Greenbaum JS, Hansen CM, Hofton MA, Holt JW, Jezek KC, Koenig LS, Kurtz NT, Kwok R, Larsen CF, Leuschen CJ, Locke CD, Manizade SS, Martin S, Neumann TA, Nowicki SM, Paden JD, Richter-Menge JA, Rignot EJ, Rodríguez-Morales F, Siegfried MR, Smith BE, Sonntag JG, Studinger M, Tinto KJ, Truffer M, Wagner TP, Woods JE, Young DA and Yungel JK (2021) The Scientific Legacy of NASA's Operation IceBridge. *Reviews of Geophysics*, **59**(2), e2020RG000712, ISSN 1944-9208 (doi: 10.1029/2020RG000712)

MathWorks (2021) Cwt

McNabb R (2025) Spymicmac. Zenodo (doi: 10.5281/zenodo.15602952)

Meier M and Post A (1969) What are glacier surges? *Canadian Journal of Earth Sciences*, **6**(4), 807–817, ISSN 0008-4077 (doi: 10.1139/e69-081)

Morin A, Flowers GE, Nolan A, Brinkerhoff D and Berthier E (2023) Exploiting high-slip flow regimes to improve inference of glacier bed topography. *Journal of Glaciology*, **69**(275), 658–664, ISSN 0022-1430, 1727-5652 (doi: 10.1017/jog.2022.121)

National Park Service (2015) Tweedsmuir Glacier Information. https://www.nps.gov/glba/learn/news/tweedsmuir-glacier-information.htm

Nolan A, Kochtitzky W, Enderlin EM, McNabb R and Kreutz KJ (2021) Kinematics of the exceptionally-short surge cycles of Sít' Kusá (Turner Glacier), Alaska, from 1983 to 2013. *Journal of Glaciology*, **67**(264), 744–758, ISSN 0022-1430, 1727-5652 (doi: 10.1017/jog.2021.29)

Nolan DM, Post AS, Hauer W, Zinck A and O'Neel S (2017) Photogrammetric scans of aerial photographs of North American glaciers (doi: 10.18739/A2VH5CJ8K)

Nuth C and Kääb A (2011) Co-registration and bias corrections of satellite elevation data sets for quantifying glacier thickness change. *The Cryosphere*, **5**(1), 271–290 (doi: 10.5194/tc-5-271-2011)

Polar Geospatial Center (2026) PGC DEM Products – ArcticDEM, REMA, and EarthDEM. Technical report

Porter C, Howat I, Noh MJ, Husby E, Khuvis S, Danish E, Tomko K, Gardiner J, Negrete A, Yadav B, Klassen J, Kelleher C, Cloutier M, Bakker J, Enos J, Arnold G, Bauer G and Morin P (2023) ArcticDEM - Mosaics, Version 4.1 (doi: 10.7910/DVN/3VDC4W)

Post A (1969) Distribution of surging glaciers in western North America. *Journal of Glaciology*, **8**(53), 229–240, ISSN 0022-1430 (doi: 10.3189/S0022143000031221)

Post A (1972) Periodic Surge Origin of Folded Medial Moraines on Bering Piedmont Glacier, Alaska. *Journal of Glaciology*, **11**(62), 219–226, ISSN 0022-1430, 1727-5652 (doi: 10.3189/S0022143000022218)

Post A and Mayo LR (1971) Glacier dammed lakes and outburst floods in Alaska. Technical Report 455, U.S. Geological Survey (doi: 10.3133/ha455)

Raup B, Racoviteanu A, Khalsa SJS, Helm C, Armstrong R and Arnaud Y (2007) The GLIMS geospatial glacier database: A new tool for studying glacier change. *Global and Planetary Change*, **56**(1), 101–110, ISSN 0921-8181 (doi: 10.1016/j.gloplacha.2006.07.018)

Raymond CF (1987) How do glaciers surge? A review. *Journal of Geophysical Research: Solid Earth*, **92**(B9), 9121–9134, ISSN 0148-0227 (doi: 10.1029/JB092iB09p09121)

RGI 70 Consortium (2023) Randolph Glacier Inventory - A Dataset of Global Glacier Outlines, Version 7.0 (doi: 10.5067/f6jmovy5navz)

Rosenholm D and Torlegård K (1988) Three-dimensional absolute orientation of stereo models using digital elevation models. **54**(10), 1385–1389

Sevestre H and Benn DI (2015) Climatic and geometric controls on the global distribution of surge-type glaciers: Implications for a unifying model of surging. *Journal of Glaciology*, **61**(228), 646–662, ISSN 0022-1430 (doi: 10.3189/2015JoG14J136)

Shean DE, Alexandrov O, Moratto ZM, Smith BE, Joughin IR, Porter C and Morin P (2016) An automated, open-source pipeline for mass production of digital elevation models (DEMs) from very-high-resolution commercial stereo satellite imagery. *ISPRS Journal of Photogrammetry and Remote Sensing*, **116**, 101–117, ISSN 0924-2716 (doi: 10.1016/j.isprsjprs.2016.03.012)

Shugar D, Flowers G, Cronmiller D, Mingo L, von Finster A and Sharp M (2024) Tweedsmuir Glacier, Alsek River, and the salmon migration that wasn't. In *European Geosciences Union General Assembly 2024 (EGU24)*, 20637 (doi: 10.5194/egusphere-egu24-20637)

Shugar DH, Kostaschuk R, Best JL, Parsons DR, Lane SN, Orfeo O and Hardy RJ (2010) On the relationship between flow and suspended sediment transport over the crest of a sand dune, Río Paraná, Argentina. *Sedimentology*, **57**(1), 252–272, ISSN 0037-0746 (doi: 10.1111/j.1365-3091.2009.01110.x)

Stein A, Huertas A and Matthies L (2006) Attenuating stereo pixel-locking via affine window adaptation. In *Proceedings 2006 IEEE International Conference on Robotics and Automation, 2006. ICRA 2006.*, 914–921, ISSN 1050-4729 (doi: 10.1109/ROBOT.2006.1641826)

Terleth Y, Bartholomaus TC, Enderlin E, Mikesell TD and Liu J (2024) Glacier Surges and Seasonal Speedups Integrated Into a Single, Enthalpy-Based Model Framework. *Geophysical Research Letters*, **51**(23), e2024GL112514, ISSN 1944-8007 (doi: 10.1029/2024GL112514)

Tober BS, Christoffersen MS, Holt JW, Truffer M and Larsen CF (2026) Alaska-Yukon Glacier Depths From a Decade of Airborne Radar Sounding. *Journal of Geophysical Research: Earth Surface*, **131**(6), e2025JF008742, ISSN 2169-9011 (doi: 10.1029/2025JF008742)

Torrence C and Compo GP (1998) A Practical Guide to Wavelet Analysis. ISSN 1520-0477

Toutin T, Schmitt C, Berthier E and Clavet D (2011) DEM generation over ice fields in the Canadian Arctic with along-track SPOT5 HRS stereo data. *Canadian Journal of Remote Sensing*, **37**(4), 429–438, ISSN 0703-8992 (doi: 10.5589/m11-052)

United States Geological Survey (2019) USGS 3D Elevation Program Digital Elevation Model

Wells A, Rounce DR and Fahnestock M (2026) Seasonal progression of melt and snowlines in Alaska from SAR reveals impacts of warming. *npj Climate and Atmospheric Science*, **9**(1), 95, ISSN 2397-3722 (doi: 10.1038/s41612-026-01321-y)

xDEM contributors (2026) xDEM (Version v0.2.0) [Computer Software]. Zenodo (doi: 10.5281/zenodo.19636034)

Young EM, Flowers GE, Jiskoot H and Gibson HD (2022) Kinematic evolution of kilometre-scale fold trains in surge-type glaciers explored with a numerical model. *Journal of Structural Geology*, **161**, 104644, ISSN 0191-8141 (doi: 10.1016/j.jsg.2022.104644)

Young TJ, Christoffersen P, Doyle SH, Nicholls KW, Stewart CL, Hubbard B, Hubbard A, Lok LB, Brennan PV, Benn DI, Luckman A and Bougamont M (2019) Physical Conditions of Fast Glacier Flow: 3. Seasonally-Evolving Ice Deformation on Store Glacier, West Greenland. *Journal of Geophysical Research: Earth Surface*, **124**(1), 245–267, ISSN 2169-9011 (doi: 10.1029/2018JF004821)

Zanaga D, Van De Kerchove R, Daems D, De Keersmaecker W, Brockmann C, Kirches G, Wevers J, Cartus O, Santoro M, Fritz S, Lesiv M, Herold M, Tsendbazar NE, Xu P, Ramoino F and Arino O (2022) ESA WorldCover 10 m 2021 v200 (doi: 10.5281/zenodo.7254221)

Supplementary Information for: Surface signatures of surge dynamics over six decades at Tweedsmuir Glacier, Saint Elias Mountains, Canada

Meghan A. SHARP,[1,2] Dan H. SHUGAR,[1], Gwenn E. FLOWERS,[3] Aram FATHIAN,[1] Friedrich KNUTH[4,5],

[1] *Water, Sediment, Hazards and Earth-surface Dynamics (WaterSHED) Laboratory, Department of Geoscience, University of Calgary, Calgary, Alberta, Canada;* [2] *Present address: College of Earth, Ocean, and Atmospheric Science, Oregon State University, Corvallis, OR, USA;* [3] *Department of Earth Sciences, Simon Fraser University, Burnaby, British Columbia, Canada;* [4] *Laboratory of Hydraulics, Hydrology and Glaciology (VAW), ETH Zurich, Zurich, Switzerland;* [5] *Swiss Federal Institute for Forest, Snow and Landscape Research (WSL), bâtiment ALPOLE, Sion, Switzerland;*
Correspondence: Meghan A. Sharp <sharpmeg@oregonstate.edu>

CONTENTS

Supplementary Figures **1**
Figure S1: ITS_LIVE velocity timeseries 2
Figure S2: Example raw images and corresponding fiducial markers 3
Figure S3: DEM Residuals 4
Figure S4: Profile locations & ice-flow direction 5

Supplementary Tables **6**
Table S1: Camera metadata and fiducial marker distances for each historical image set . . 6

SUPPLEMENTARY FIGURES

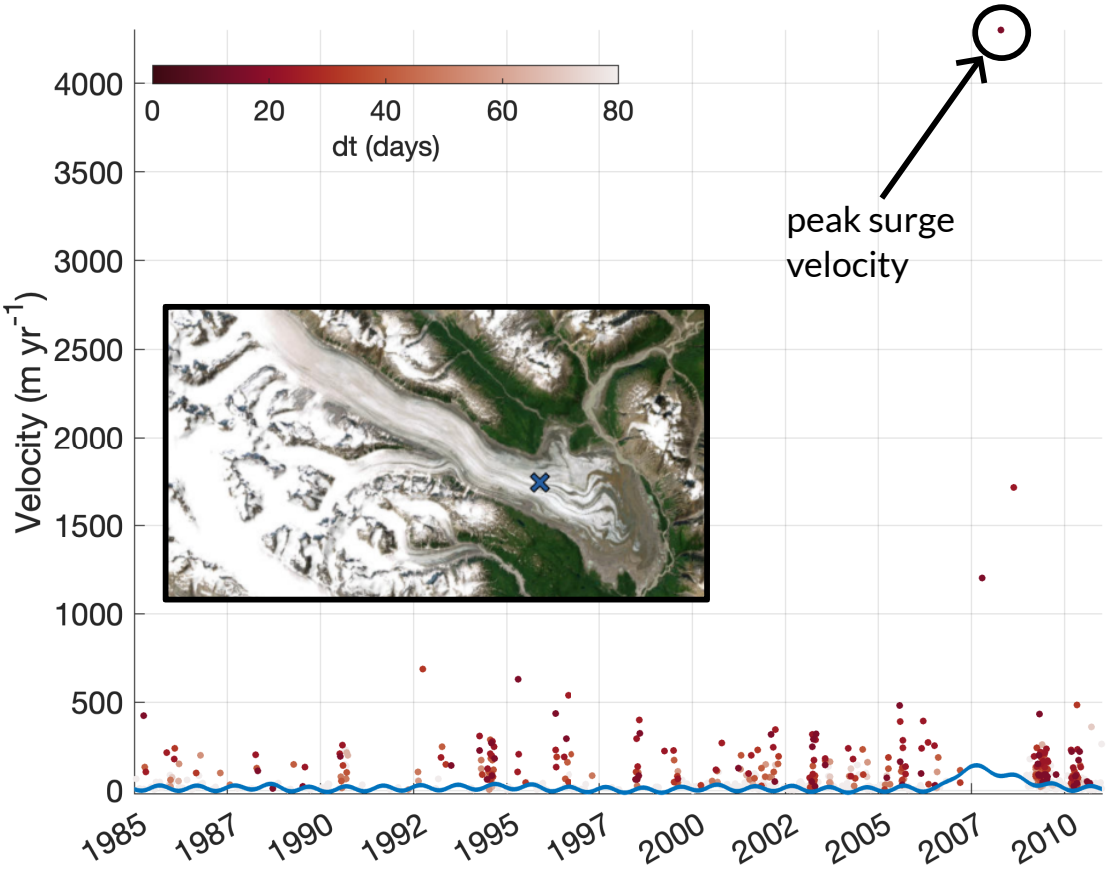


Fig. S1: ITS_LIVE velocity timeseries for Tweedsmuir Glacier at the location marked in the inset map (59.8055°N, -138.0841°E). Blue line denotes annual composite velocities and circles denote individual image pair measurements coloured by the time between image acquisitions. Figure produced with the ITS_LIVE MATLAB repository (https://github.com/chadagreene/ITS_LIVE)

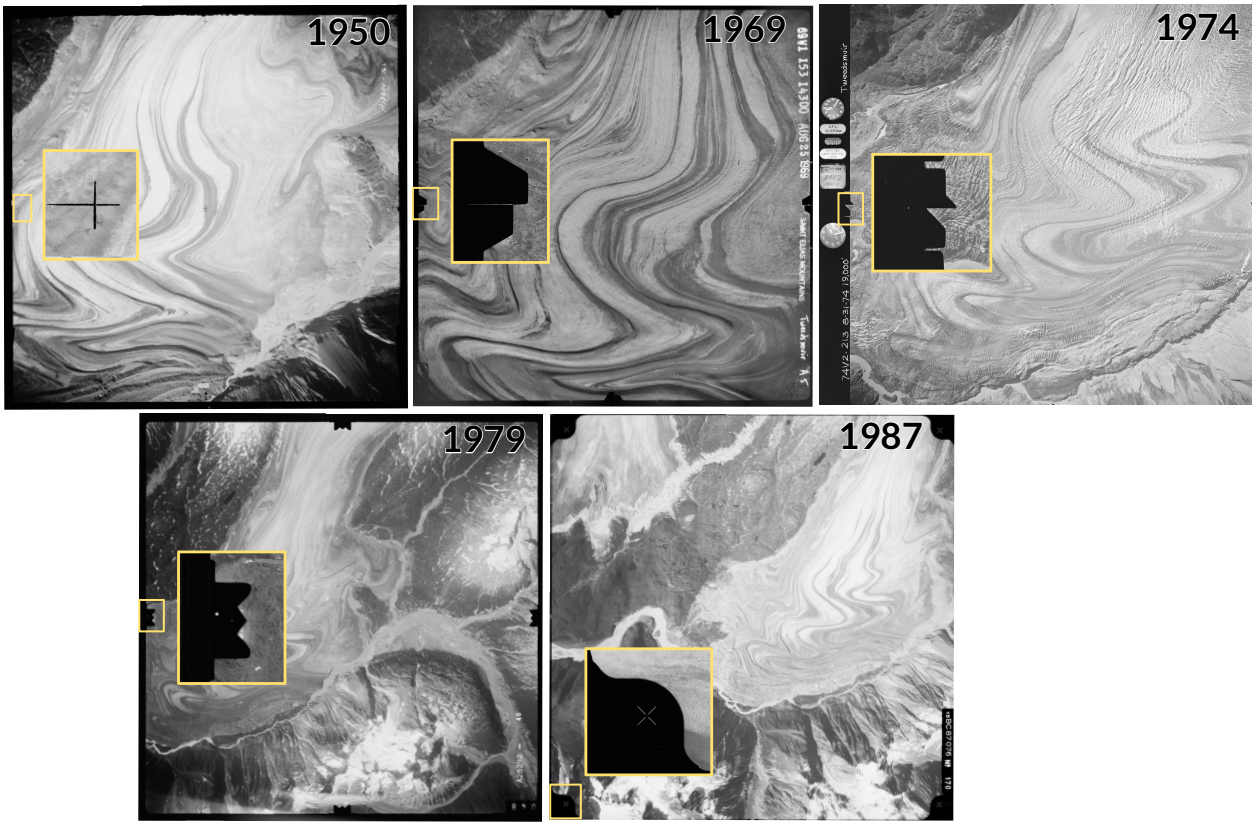


Fig. S2: Example raw images and corresponding fiducial markers for each image set. See Figure 3 in Knuth and others (2023) for examples of pseudofiducial markers.

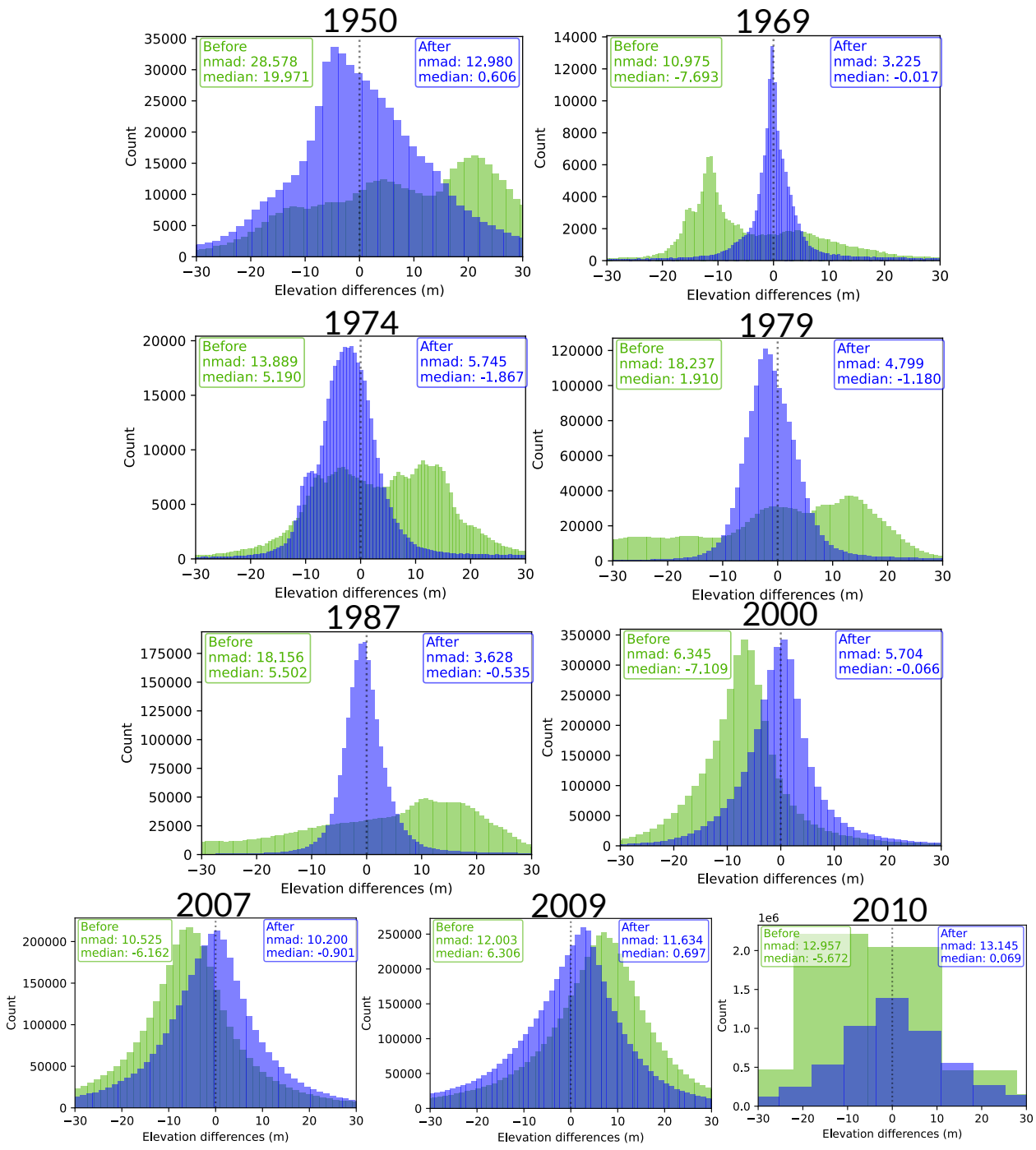


Fig. S3: Residuals between the reference DEM (Arctic DEM) and historical and SPOT5 DEMs ofer stable terrain before and after co-registration.

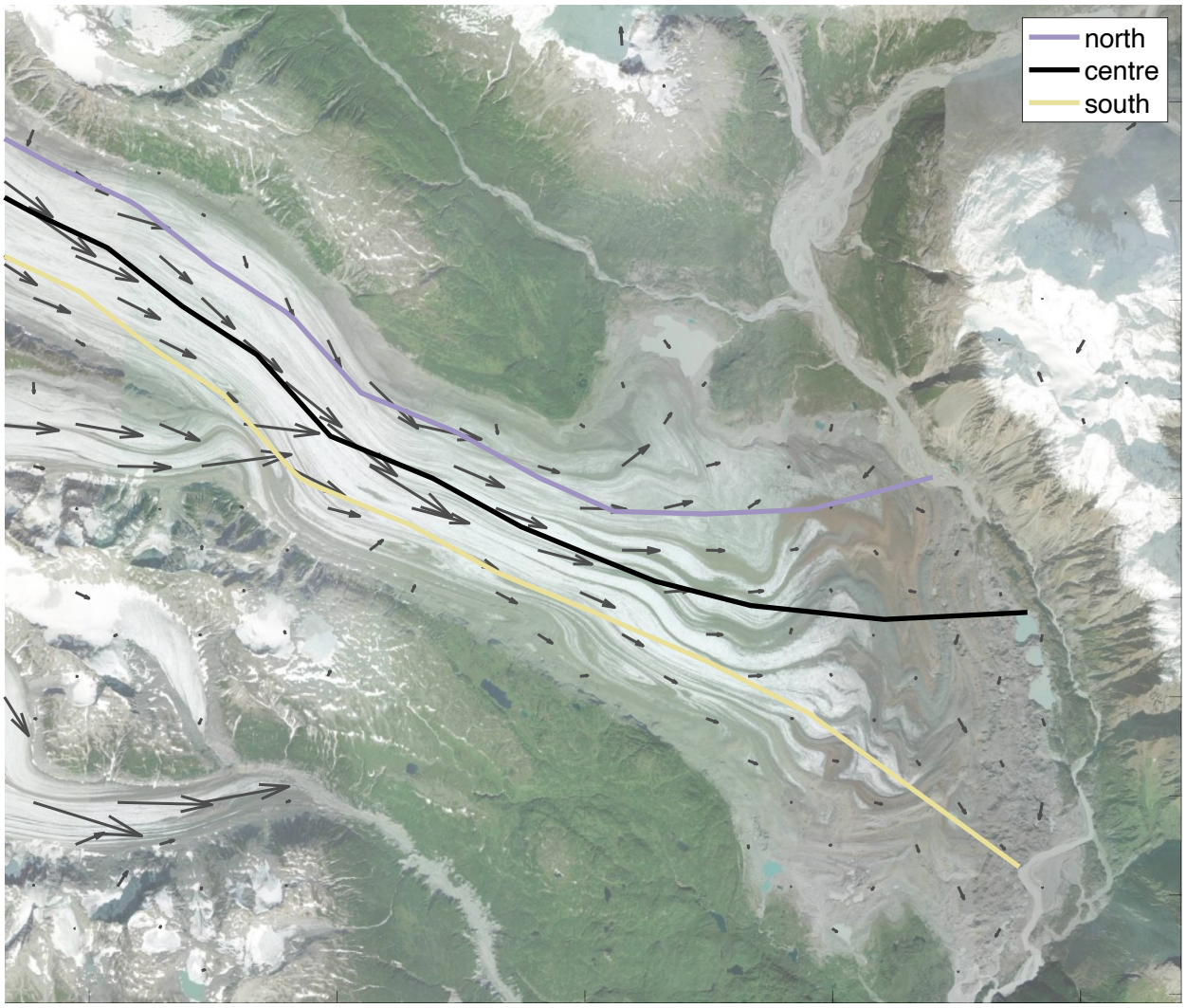


Fig. S4: ITS_LIVE composite velocity field (black arrows) for Tweedsmuir Glacier and location of elevation profiles used in this study. Figure produced with the ITS_LIVE MATLAB repository (https://github.com/chadagreene/ITS_LIVE)

SUPPLEMENTARY TABLES

Table S1: **Camera metadata and fiducial marker distances for each historical image set.** Sources indicate the library that scans were obtained from (NAPL = Canadian National Air Photo Library; NAGAP = USGS North American Glacier Aerial Photography archive; UAF = University of Alaska Fairbanks; GeoBC = British Columbia GeoBC Image Library). Midside distances are measured left–right (L–R) and top–bottom (T–B); corner distances are measured along the bottom-left–top-right (BL–TR) and top-left–bottom-right (TL–BR) diagonals and pseudo = images with pseudofiducials. * denotes fiducial distances estimated from mean marker positions.

Acquisition date (yyyy-mm-dd)	Source	Roll	Camera type	Nominal focal length (mm)	Scanning resolution (μm)	Pre-processed square image dimensions (pixels)	Midside fiducial distance (mm)		Corner fiducial distance (mm)	
							L–R	T–B	BL–TR	TL–BR
1950										
1950-07-03	NAPL	A12819	Williamson OSC	152.950	12.4	17712	220.057*	220.143*	302.025*	302.444*
1950-07-18	NAPL	A12820	Williamson OSC	153.850	12.4	17712	220.057*	220.143*	302.025*	302.444*
1950-02-15	NAPL	A12850	Williamson OSC	152.650	12.4	17712	220.191*	220.196*	302.478*	302.455*
1950-07-18	NAPL	A12852	Williamson OSC	153.850	12.4	17712	220.040*	220.047*	302.098*	302.688*
1950-07-03	NAPL	A12856	Williamson OSC	152.950	12.4	17712	220.057*	220.143*	302.025*	302.444*
1969										
1969-08-25	NAGAP/UAF	69V1	Unknown	151.283	20.0	17552	pseudo	pseudo	–	–
1974										
1974-08-31	NAGAP	74V2	Unknown	151.283	20.0	11270	pseudo	pseudo	–	–
1979										
1979-08-21	NAPL	A25291	Zeiss RMK A	153.370	12.4	15128	226.010	225.986	–	–
1979-08-22	NAPL	A25292	Zeiss RMK A	153.370	12.4	15128	226.010	225.986	–	–
1979-08-22	NAPL	A25293	Zeiss RMK A	153.370	12.4	15128	226.010	225.986	–	–
1987										
1987-08-24	GeoBC	bc87076	Wild RC8	152.262	12.0	15624	–	–	299.813	299.818

REFERENCES

Knuth F, Shean D, Bhushan S, Schwat E, Alexandrov O, McNeil C, Dehecq A, Florentine C and O'Neel S (2023) Historical Structure from Motion (HSfM): Automated processing of historical aerial photographs for long-term topographic change analysis. *Remote Sensing of Environment*, **285**, 113379, ISSN 0034-4257 (doi: 10.1016/j.rse.2022.113379)